"Energy Systems and Nanotechnology" - Advances in Sustainability Science and Technology Book Series, Springer, Editors: D. Tripathi and R. Sharma, In press for April (2021).

Invited Book Chapter

Accepted November 5th 2020

Thermal analysis of $\gamma Al_2O_3/H_2O$ and $\gamma Al_2O_3/C_2H_6O_2$ elastico-viscous nanofluid flow driven by peristaltic wave propagation with electroosmotic and magnetohydrodynamic effects: *Applications in nanotechnological energy systems*

[1]J. Prakash, [*2]D. Tripathi and [3]O. Anwar Bég

*[1]Department of Mathematics, Avvaiyar Government College for Women, Karaikal-609 602, Pondicherry –U.T., **India.***

*[2]Department of Mathematics, National Institute of Technology Uttarakhand, Srinagar -246174, **India***

*[3]Multi-Physical Engineering Sciences Group, Department of Mechanical and Aeronautical Engineering, SEE, Salford University, M54WT, England, **UK.***

[*]Corresponding author. E-mail: dtripathi@nituk.ac.in (D. Tripathi)

ABSTRACT

Motivated by new developments in electromagnetic nano/microfluidic energy systems, in this chapter a novel study is described of the thermal performance in unsteady peristaltic electro-osmotic hydromagnetic viscoelastic (Jeffreys model) flow of water based-γAl_2O_3 nanofluids and ethylene glycol-based γAl_2O_3 nanofluids in a microchannel. The flow is governed by single wave propagation of the microchannel walls which is further controlled by the electroosmosis mechanism with electrical double layer effects. Magnetic field effect and Joule electrical dissipation are also considered in the flow analysis. The two-dimensional governing equations are transformed into non-dimensional form and further simplified using small Reynolds number (*Re*) and long wavelength ($\delta \ll 1$) assumptions. The Poisson-Boltzmann equation is deployed to describe the ionic distribution via Debye-Hückel linearization. The variations in axial pressure gradient, axial velocity and temperature distribution for different electrical, magnetic and nanoscale flow parameters are computed and visualized graphically. The findings of the present computations in the optimization of many emerging applications in energy systems nanotechnology including micro/nano pumping devices, electromagnetic nano-energy harvesting, thermal control of biomimetic microfluidics, nanomedicine etc.

KEYWORDS: *Electroosmosis; Magnetic field; single wave propagation; Jeffery viscoelastic fluid; γAl_2O_3 nanoparticles; Energy nanotechnology; Debye-Hückel linearization; Hartmann number; heat transfer.*

1. INTRODUCTION

Nanotechnology has emerged as the most significant branch of modern industry in the 21st century owing to the unique capabilities it provides in fabricating new structures at the atomic scale [1]. This has witnessed an explosion in the synthesis of novel materials and devices which have filtered into numerous areas of engineering. Important applications include sustainable fuel cells and plasmonic-biovoltaic cells [2], photobioreactor technology [3], microelectrochemical reactors and energy conversion systems [4] and nano/microfluidic power plant for spacecraft [5]. An important sub-branch of nanomaterials is nanofluids. *Nanofluids* refer to colloidal suspensions of ultrafine nanometer-sized particles dispersed in base fluids (water, greases, de-ionized water, ethylene glycol, silicon oil and poly-α-olefin oil (PAO) etc). They were introduced for engineering heat transfer applications at Argonne energy laboratory, US department of energy in the 1990s and are elaborated in great detail by Das *et al.* [6]. Generally nanoparticles are synthesized from metals (Cu, Ag), Carbides (Sic), oxides (TiO_2, Al_2O_3) or non-metallic carbon nanotubes. Many different mathematical models have been proposed to account for the exceptional convective heat transport observed in nanofluids including ballistic collisions due to random (haphazard) Brownian motion, thermophoresis, micro-convection etc [7]. Nanofluids have therefore been embraced in an impressive range of energy, transport and biomedical technologies including compression ignition power plants [8], passive thermal storage systems [9], vacuum flash evaporation [10], automotive waste heat recovery and coolant systems [11], nuclear reactors [12], rotating disk reactors [13], lubrication systems for heat dissipation [14] and anti-corrosion [15], nano-pharmacological delivery [16], laser treatment of nanoparticle doped hyperthermia treatments [17], smart coating systems [18-20], solar energy direct absorber and photovoltaic collectors [21-26], polymer electrolyte membrane (PEM) fuel cells [27] and biological nanofluid fuel cells for marine engineering [28]. All these applications have confirmed the superior performance of nanofluids compared with conventional engineering fluids.

In parallel with nanofluid developments in energy sciences, the field of *electro-osmotic fluidics* (EOF) has also witnessed considerable interest in recent years. Electroosmotic flow [29] is the bulk liquid motion mobilized when an externally applied electric field interacts with the net surplus of charged ions in the diffuse part of an electrical double layer (EDL). Electroosmotic fluid dynamics is a special case of the more general area of electro-kinetics [30]. Intrinsic to

electroosmotic flow efficiency is the electrical double layer which constitutes a very thin region of nonzero net charge density near a two-phase interface (e.g. a solid-liquid interface). It is produced by the adsorption or desorption of charged species from the surface and the resulting rearrangement of the local free ions in solution so as to maintain overall electroneutrality. In recent years there has been a resurgence in interest in electro-osmotic fluidics, largely due to the potential envisaged in mechanical energy conversion (e.g. electrokinetic pumps) and mechanically pumped flow for direct electrical energy conversion (via the streaming potential) in addition to novel electroosmotic cell materials developments. Important studies in this regard include Yang *et al.* [31] (electro-osmotic microchannel batteries) and Daiguji *et al.* [32] (on electro-chemo-mechanical nanofluidic channel energy generation). Numerical and analytical studies of electro-osmotic transport in microchannels have also received some attention. Jian *et al.* [33] developed analytical power series solutions for the oscillatory EOF flow of the generalized Maxwell fluids through a two-dimensional rectangular microchannel. Ali *et al*. [34] derived closed form solutions for two-fluid electro-osmotic wavy flow through a cylindrical tube with hydrodynamic wall slip and shear-thinning effects.

Magnetohydrodynamics (MHD) has also stimulated considerable interest in energy sciences in recent decades [35]. MHD involves the interaction between the electric currents and magnetic fields in either inviscid or viscous flow which results in Lorentz body forces that can be used to propel and manipulate fluids. Both direct and alternating currents may be utilized in MHD. The enclosing walls i.e. electrodes in MHD power systems must be carefully designed. In direct current systems, electrodes may be damaged by electrochemistry generating bubble formation and electrode corrosion [36]. However direct current systems have the advantage that they mitigate the parasitic eddy currents associated with alternating currents that can produce excessive heating. MHD also offers some advantages over purely electroosmotic systems since much lower electrode potentials (< 1Volt) can be used and produce superior volumetric flow rates, provided the conduit dimensions are not excessively small. Furthermore, in MHD power systems, only working fluid is circulated, and there is an absence of moving mechanical parts which greatly decreases the mechanical losses which are typically much higher in conventional power generation systems [37]. MHD has therefore been implemented in many energy systems including MHD thermal micropumps [38], Hall generators [39], magnetic microfluidics for rocket propulsion [40], cilia generated propulsion in magnetic field regulation of multiphase heat transfer [41], running liquid

MHD chromatography biochemical analysis systems [42], pumping of magnetized slurries in biochemical engineering [43], intelligent materials processing [44], magnetic polymer pumping [45], ocean MHD wave energy generation [46], NMR actuation [47], plasma control in nuclear reactor ducts [48], magneto-micro-bio-robotic propulsion [49], thermodynamic optimization of MHD bypass systems [50], magnetic field control of geological oil spills [51] and magnetic field manipulation of external enrobing deposition processes on aerospace components [52]. Mathematical models of MHD flows generally involve the modification of the Navier-Stokes equations with supplementary magnetic body forces, and in some cases extra balance equations for magnetic induction.

The combined use of electrical and magnetic fields in viscous fluid dynamics has also garnered some attention. The dual deployment of both electrical and magnetic fields offers unique advantages which are not achievable with either field separately. Jian *et al.* [53] used analytical methods to study the unsteady rotating electromagnetohydrodynamic (EMHD) flow of an electrically conducting, incompressible and viscous fluid between two slit microparallel plates, in the presence of an externally imposed electrical current and a transverse magnetic field. They observed a substantial boost in flow rates both in axial and in lateral directions due to the assisting component of Lorentz force being significantly larger than the inhibiting component for a specific range of phase of the magnetic field relative to the electrical field. Tso and Sundaravadivelu [54] derived analytical solutions for the influence of orthogonal electrical and magnetic electromagnetic fields on the surface tension driven capillary flow in a microchannel, noting that , with strong magnetic field, the application of electric current boosts fluid flow rates and decreases the time taken to fill the microchannel length relative to the non-magnetic case. Further interesting studies of composite electrical and magnetic field effects on conducting viscous flows include Si and Jian [55] for wavy wall micropumps, Buren and Jian [56] (for wavy electrophoresis microchannel systems) and Nguyen [56] (on microscale electro-magneto-fluidic devices for medical and biotechnology applications).

Engineers have also investigated the combination of nanofluids and electromagnetic fields in hybrid systems. In such systems, base fluids are doped with electromagnetic nanoparticles which can be manipulated by external electrical and magnetic fields. Important studies in this regard include Zhao *et al.* [57] who studied magnetic nano-doped microchannels. Combined

electroosmotic magnetohydrodynamic nanofluid flows in chemical ducts were examined by Ganguly and Sarkar [59]. They showed that under axial electrical field and transverse magnetic field, increasing Hartmann number (magnetic body force parameter) suppresses advective transport of the liquid and heat transfer whereas greater nanoparticle volume fraction, nanoparticle size and Joule electrothermal dissipation all elevate temperature. Further studies have been communicated by Sarkar and Ganguly [60] (with pressure gradient effects), Zhao *et al.* [61] (including Brinkman dissipation effects) and Thumma *et al.* [62] (on external magnetic nanofluid viscous flow with, gravitational, heat generation and absorption effects).

Increasingly modern engineering designs are featuring bio-inspired adaptive characteristics. These include biophysical adhesives for enhanced integrity, surface protuberances for turbulence control (e.g. leading edge break up devices in morphing aerodynamics), compliant surfaces for drag control, and physiological propulsion mechanisms. An extremely efficient natural mechanism for both internal and external propulsion is peristalsis [63]. For example, in gastric transport, this refers to the rhythmic involuntary movements (progressive wavelike contractions) of the longitudinal and circular muscles. It can also arise in swallowing in the esophagus, blood flow etc. The waves can be short, local reflexes or long, continuous contractions that travel the whole length of the vessel, depending upon their location and what initiates their action. Peristalsis has been adopted very successfully also in modern pump design [64], for example in medical dosing systems and chemical waste transits which require low flow rates and pressure and operate on the suction-compression created by rotors on a silicone tube, commonly used for simple dosing application. Such pumps are basically a type of positive displacement **pump** and can be deployed for conveying a variety of toxic fluids, do not require seals, valves or moving parts in the flow path, and eliminate the risk of clogging, leaking or contamination. Peristaltic propulsion also features in internal water transport in green plants [65], embryonic hemodynamics [66, 67], larva locomotion [68], leech crawling [69], robot locomotion [70], respiration [71], digestive transport [72], botanical translocation of phloem/xylem [73], vasomotion (periodic oscillations of blood vessels walls) in bat wings [74], bile dynamics [75] and chyme mixing processes in intestinal fluid mechanics [76]. Many mathematical studies of peristaltic flows have been communicated which usually employ the lubrication theory approximations to render the conservation equations more amenable for exact or computational solutions. They also focus on the key aspects of bolus dynamics and trapping (reflux) phenomena. Relevant works in this regard include Yih and Fung

[77], Bertuzzi and Salinari [78] (both of which considered Newtonian fluids), Bohme and Friedrich [79] (elastic-viscous fluids), Takabatake *et al.* [80] (hydromechanical pumping efficiency), Jiménez-Lozano and Sen [81] (streamline topologies and bifurcation analysis), Ehsan *et al.* [82] (dynamic systems modelling of peristaltic waves) and Bég *et al.* [83] (fluid-structure interactional computational modelling of peristaltic viscoplastic pumping). In the past decade or so, researchers have also explored electromagnetic peristaltic flows, for a variety of working fluids including Newtonian magnetic nanofluids, magnetic non-Newtonian polymers, electroconductive liquids etc. Interesting studies in this area include Prakash et al. [84] who developed a comprehensive mathematical model for solar magnetohydrodynamic nanofluid peristaltic pumps. Narla *et al.* [85] investigated unsteady magneto-rheological polymer pumping in curved conduits. Electroosmotic peristaltic transport has received some attention owing to applications in biomechanics and microfluidic energy systems. Narla *et al.* [86] presented a detailed theoretical and computational study of non-Newtonian embryological peristaltic electro-osmotic dynamics. Tripathi *et al.* [87] derived analytical solutions for electro-osmotic transport in Darcian porous media under peristaltic waves. Tripathi *et al.* [88] studied the propulsion of aqueous ionic couple stress Stokesian fluids under axial electrical field in a deformable microchannel. Electro-osmotic microchannel nanofluid transport has also been investigated by Tripathi *et al.* [89, 90] using Buongiorno two-component nanoscale models and by Prakash *et al.* [91] using modified hybrid Tiwari-Das nanoparticle models. Further studies have verified the considerable advantages of simultaneously deploying electrical and magnetic fields for beneficially manipulating microchannel transport phenomena. Some recent works in this regard include Tripathi *et al.* [92] for Newtonian aqueous liquids, Tripathi *et al.* [93] for couple stress rheological ionic fluids and Prakash *et al.* [94] for Newtonian slip electromagnetic nanofluid radiative convective flow.

In the present chapter, we consider *transient peristaltic electro-osmotic hydromagnetic viscoelastic flow of water based-γAl_2O_3 nanofluids and ethylene glycol-based γAl_2O_3 nanofluids in a microchannel, under the action of mutually orthogonal electrical (axial) and magnetic (transverse) fields*. Such nanofluids have been shown to offer great promise in thermal ducts and energy optimization [95-98]. Modern bio-inspired micro/nano-fluidic energy systems are increasingly utilizing rheological fluent characteristics to refine designs and improve efficiencies [99]. Lu *et al.* [100] have further demonstrated that viscoelastic ionic liquids avoid the constriction in focused particle streams which arises in a direct current electric fields for conventional

Newtonian fluids. They have also demonstrated that particle aggregations can be sustained at relatively high electric fields and can be manipulated more effectively in viscoelastic media than Newtonian media. It is therefore very beneficial to analyse viscoelastic electro-osmotic dynamics in such systems. A wide spectrum of excellent viscoelastic models are available for robust simulations in this regard and include the Maxwell model, Reiner-Rivlin differential third grade model, Phan-Thein-Tanner (PTT) model and fractional Maxwell model. In different viscoelastic models, a variety of convected derivatives are deployed. For example, the Upper convected Maxwell (UCM) fluid uses an upper convected derivative whereas the lower convected Maxwell (LCM) fluid uses the lower convected derivative. The Johnson-Segalman fluid employs a linear combination of upper convected and lower convected derivatives and is popular for *shear-banding*. An alternative model is the *Jeffreys elastico-viscous model* [101] which accurately simulates many industrial, biophysical and thermal processing fluids and features three constants i.e. viscosity at zero shear rate, and two time-related material parameter constants (for stress relaxation and retardation time). Jeffrey's fluid model can be reduced to the classical Newtonian fluid when shear stresses are high near the walls. Such fluids exhibit shear thinning properties and high shear rate viscosity. Jeffreys model has been applied widely in micro/nano scale fluid dynamics and bionics [102-104] and is therefore utilized in the present analysis. The Tiwari-Das nanoscale model is employed. Via lubrication approximations the conservation equations are reduced, and a Poisson-Boltzmann equation is deployed to describe the ionic distribution via Debye-Hückel linearization. Extensive graphical illustrations are produced using MATLAB symbolic software for axial pressure gradient, axial velocity and temperature distributions with different electrical, magnetic and nanoscale flow parameters for water based-γAl_2O_3 nanofluids and ethylene glycol-based γAl_2O_3 nanofluids. Detailed interpretation of the results is provided with future pathways for extensions of the current modelling.

2. MATHEMATICAL MODEL

2.1. Single wave propagation

The proposed geometric model for the magnetohydrodynamic electro-osmotic flow of $\left(\gamma Al_2O_3 / H_2O,\ \gamma Al_2O_3 / C_2H_6O_2\right)$ nanofluids induced by the single wave peristaltic propagation along microchannel walls is sketched in **Fig.1.** It is mathematically expressed as:

$$\bar{H}\left(\bar{X},\bar{t}\right)=\begin{cases} d-\bar{a}\cos^2\left[\dfrac{\pi}{\lambda}\left(\bar{X}-c\bar{t}\right)\right] & if\ \ \bar{t}<\bar{X}<\bar{t}+1 \\ d-\bar{a}, & if\ \ \bar{X}\in\left[0,t\right]\cup\left[t+1,\,L\right] \end{cases}. \tag{1}$$

in which d , $\bar{a}$, c, λ and $\bar{t}$ symbolize the width of the microchannel, amplitude of the wave, wave speed, the wavelength and time respectively

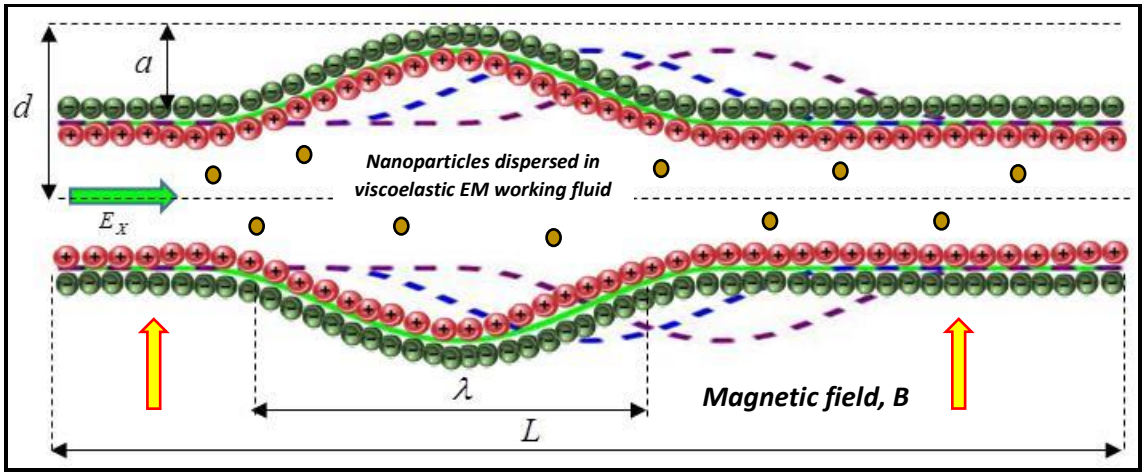

Fig.1 Electroosmotic magnetohydrodynamic nanofluid peristaltic flow in microchannel

2.2. Governing equations for convective Jeffery nanofluid model

The stress-strain relationship for the Jeffery fluid model is considered as:

$$\bar{\tau}=\frac{\mu_{eff}}{1+\lambda_1}\left(\dot{\gamma}+\lambda_2\ddot{\gamma}\right), \tag{2}$$

in which μ_{eff} is the effective viscosity, λ_1 is the ratio of the relaxation time to retardation time (Jeffery parameter), λ_2 the retardation time, $\dot{\gamma}$ the shear rate and dots over the quantities denote differentiation with respect to time. The relevant flow equations for mass, momentum and energy conservations are as follows [94] neglecting magnetic induction effects:

$$\frac{\partial\bar{U}}{\partial\bar{X}}+\frac{\partial\bar{V}}{\partial\bar{Y}}=0, \tag{3}$$

$$\rho_{nf}\left(\frac{\partial\bar{U}}{\partial\bar{t}}+\bar{U}\frac{\partial\bar{U}}{\partial\bar{X}}+\bar{V}\frac{\partial\bar{U}}{\partial\bar{Y}}\right)=-\frac{\partial\bar{P}}{\partial\bar{X}}+\frac{\partial\bar{\tau}_{\bar{X}\bar{X}}}{\partial\bar{X}}+\frac{\partial^2\bar{\tau}_{\bar{Y}\bar{X}}}{\partial\bar{Y}}-\bar{U}\bar{\sigma}_{nf}\bar{B}_0^2+\rho_e\bar{E}_X+g\left(\rho\beta\right)_{nf}\left(\bar{T}-T_m\right), \tag{4}$$

$$\rho_{nf}\left(\frac{\partial \bar{V}}{\partial \bar{t}}+\bar{U}\frac{\partial \bar{V}}{\partial \bar{x}}+\bar{V}\frac{\partial \bar{V}}{\partial \bar{Y}}\right)=-\frac{\partial \bar{P}}{\partial \bar{Y}}+\mu_{nf}\left(\frac{\partial \bar{\tau}_{\bar{X}\bar{Y}}}{\partial \bar{X}}+\frac{\partial \bar{\tau}_{\bar{Y}\bar{Y}}}{\partial \bar{Y}}\right)-\bar{V}\bar{\sigma}_{nf}B_0{}^2, \tag{5}$$

$$\left(\rho c_p\right)_{nf}\left(\frac{\partial \bar{T}}{\partial \bar{t}}+\bar{U}\frac{\partial \bar{T}}{\partial \bar{X}}+\bar{V}\frac{\partial \bar{T}}{\partial \bar{Y}}\right)=\kappa_{nf}\left(\frac{\partial^2 \bar{T}}{\partial \bar{X}^2}+\frac{\partial^2 \bar{T}}{\partial \bar{Y}^2}\right)+\bar{\sigma}_{nf}\bar{E}_X^2. \tag{6}$$

$$\bar{\tau}_{\bar{X}\bar{X}}=\frac{2\mu_{nf}}{1+\lambda_1}\left[1+\lambda_2\left(\bar{U}\frac{\partial}{\partial \bar{X}}+\bar{V}\frac{\partial}{\partial \bar{Y}}\right)\right]\frac{\partial \bar{U}}{\partial \bar{X}}, \tag{7}$$

$$\bar{\tau}_{\bar{X}\bar{Y}}=\bar{\tau}_{\bar{Y}\bar{X}}=\frac{\mu_{nf}}{1+\lambda_1}\left[1+\lambda_2\left(\bar{U}\frac{\partial}{\partial \bar{X}}+\bar{V}\frac{\partial}{\partial \bar{Y}}\right)\right]\left(\frac{\partial \bar{U}}{\partial \bar{Y}}+\frac{\partial \bar{V}}{\partial \bar{X}}\right), \text{ and} \tag{8}$$

$$\bar{\tau}_{\bar{Y}\bar{Y}}=\frac{2\mu_{nf}}{1+\lambda_1}\left[1+\lambda_2\left(\bar{U}\frac{\partial}{\partial \bar{X}}+\bar{V}\frac{\partial}{\partial \bar{Y}}\right)\right]\frac{\partial \bar{V}}{\partial \bar{Y}}. \tag{9}$$

Here $\bar{U}$ and $\bar{V}$ are the axial and transverse velocity components in the $\bar{X}$ and $\bar{Y}$ directions respectively, ρ_{nf}, $\partial/\partial\bar{t}$, $\bar{P}$, μ_{nf}, $\bar{E}_X$, $\left(c_p\rho\right)_{nf}$, $\bar{T}$, κ_{nf}, B_o, and $\bar{\sigma}_{nf}$ are the effective density of the nanofluid, material time derivative, pressure, effective viscosity of the viscoelastic nanofluid, axially-applied electric field, effective heat capacity of the nanofluid, temperature, effective thermal conductivity of the nanofluid, magnetic field and effective electrical conductivity respectively.

2.3. Electro-osmotic hydrodynamics

The Poisson equation with electric potential $\tilde{\Phi}$ is given by:

$$\rho_e=-\varepsilon_{ef}\nabla^2\tilde{\Phi}, \tag{10}$$

here ε_{ef} is the dielectric constant and $\rho_e=ze\left(\bar{n}_+-\bar{n}_-\right)$, is net charge density, in which *z* and *e* are the charge balance and electron charge, $\bar{n}_-$ and $\bar{n}_+$ represent negative and positive ions having bulk concentration n_o. The Boltzmann distribution is derived as:

$$\rho_e=-2n_0ez\sinh\left(\frac{ez\tilde{\Phi}}{k_BT_m}\right), \tag{11}$$

in which k_B and T_m are the Boltzmann constant and absolute temperature respectively.

2.4. Physical characteristics of $\left(\gamma Al_2O_3/H_2O,\ \gamma Al_2O_3/C_2H_6O_2\right)$ *nanofluids*

The physical characteristics of nanofluids $\left(\gamma Al_2O_3/H_2O,\ \gamma Al_2O_3/C_2H_6O_2\right)$ are as follows [95-98]:

(i) The effective dynamic viscosity is $\rho_{nf}=\rho_{bf}\left(1-\chi\right)+\chi\rho_s$

(ii) The effective heat capacitance is $\left(\rho c_p\right)_{nf}=\chi\left(\rho c_p\right)_s+\left(\rho c_p\right)_{bf}\left(1-\chi\right)$

(iii) The coefficient of thermal expansion is $\left(\rho\beta\right)_{nf}=\chi\left(\rho\beta\right)_s+\left(\rho\beta\right)_{bf}\left(1-\chi\right)$

(iv) The effective electrical conductivity is $\sigma_{nf}=\sigma_{bf}\left(1+\dfrac{3\left(\sigma-1\right)\chi}{\sigma+2-\left(\sigma-1\right)\chi}\right)$,

here $\sigma=\sigma_s/\sigma_{bf}$.

(v) The dynamic viscosity of the $\left(\gamma Al_2O_3-H_2O\right)$nanofluid is $\mu_{nf}=\mu_{bf}\left(123\chi^2+7.3\chi+1\right)$.

(vi) The dynamic viscosity of the $\left(\gamma Al_2O_3-C_2H_6O_2\right)$nanofluid is $\mu_{nf}=\mu_{bf}\left(306\chi^2-0.19\chi+1\right)$.

(vii) The effective thermal conductivity of the $\left(\gamma Al_2O_3-H_2O\right)$nanofluid is $\kappa_{nf}=\kappa_{bf}\left(4.97\chi^2+2.72\chi+1\right)$.

(viii) The effective thermal conductivity of the $\left(\gamma Al_2O_3-C_2H_6O_2\right)$nanofluid is $\kappa_{nf}=\kappa_{bf}\left(28.905\chi^2+2.8273\chi+1\right)$.

(ix) The effective Prandtl number of the $\left(\gamma Al_2O_3-H_2O\right)$nanofluid is $\mathrm{Pr}_{nf}=\mathrm{Pr}_{bf}\left(82.1\chi^2+3.9\chi+1\right)$.

(x) The effective Prandtl number of the $\left(\gamma Al_2O_3-C_2H_6O_2\right)$nanofluid is $\mathrm{Pr}_{nf}=\mathrm{Pr}_{bf}\left(254.3\chi^2-3\chi+1\right)$.

Here $\rho_{bf},\rho_s,\chi,\left(c_p\right)_{bf},\left(c_p\right)_s,\beta_{bf},\beta_s,\sigma_{bf},\sigma_s,\kappa_{bf},\mu_{bf}$ and Pr_{bf} represent the density of base fluid, density of nanoparticle, solid fractional volume of nanofluid, specific heat of base fluid, specific heat of nanoparticle, base fluid thermal expansion coefficient, nanoparticle thermal expansion coefficient, electrical conductivity of base fluid, electrical conductivity of

nanoparticle, thermal conductivity of base fluid, dynamic viscosity of base fluid and Prandtl number base fluid.

Table – 1: Thermo-physical characteristics of water, ethylene glycol and alumina.

Physical properties	Pure water (H_2O)	Ethylene glycol $(C_2H_6O_2)$	Alumina (Al_2O_3)
$\rho(kg/m^3)$	998.3	1116.6	3970
$c_p(J/kgK)$	4182	2382	765
$\kappa(W/mK)$	0.60	0.249	40
σ_s	10^{-12}	10^{-12}	
σ_f	0.05	1.07×10^{-7}	
$\beta\times10^{-5}(K^{-1})$	20.06	65	0.85
Pr	6.96	204	--

3. SCALING ANALYSIS AND BOUNDARY CONDITIONS

The following dimensionless variables are introduced:

$$x=\frac{\bar{X}}{\lambda},y=\frac{\bar{Y}}{d},t=\frac{c\bar{t}}{\lambda},u=\frac{\bar{U}}{c},v=\frac{\bar{V}}{\delta c},\delta=\frac{d}{\lambda},p=\frac{d^2\bar{P}}{c\lambda\mu_{bf}},\mathrm{Re}=\frac{\rho_{bf}cd}{\mu_{bf}},\Phi=\frac{\tilde{\Phi}}{\varsigma},$$

$$H=B_0\,d\sqrt{\sigma_{bf}/\mu_{bf}},U_{HS}=-\frac{\mathbf{E}_x\varepsilon_{ef}\varsigma}{c\mu_{bf}},Gr=\frac{g(\rho\beta)_f(T_1-T_0)d^2}{c\mu_{bf}},\theta=\frac{\bar{T}-T_0}{T_1-T_0}, \tag{12}$$

$$\kappa=ez\sqrt{\frac{2n_0}{\varepsilon k_BT_m}},\ \mathrm{Pr}_{nf}=\frac{\mu_{bf}(c_p)_{bf}}{\kappa_{bf}},\gamma=\frac{\sigma_{bf}d^2\mathbf{E}_x^2}{\kappa_{bf}(T_1-T_0)},h=\frac{\bar{H}}{d},a=\frac{\bar{a}}{d},\tau=\frac{\bar{\tau}d}{\mu_{bf}c}.$$

Eqn. (11) is transformed as:

$$\frac{\partial^2\Phi}{\partial y^2}=\kappa^2\sinh(\Phi). \tag{13}$$

Applying the lubrication (low Reynolds number and large wavelength number) approximations, Eqns. (1) and (3)-(9) are therefore scaled as follows:

Case (i) $\left(\gamma Al_2O_3 - H_2O\right)$ ***nanofluid***

$$\frac{\partial u}{\partial x}+\frac{\partial v}{\partial y}=0, \tag{14}$$

$$\frac{\partial p}{\partial x}=\frac{\left(123\chi^2+7.3\chi+1\right)}{1+\lambda_1}\frac{\partial^2 u}{\partial y^2}-H^2\left(1+\frac{3(\sigma-1)\chi}{\sigma+2-(\sigma-1)\chi}\right)u+U_{HS}\frac{\partial^2\Phi}{\partial y^2} + Gr\left(\chi\frac{(\rho\beta)_s}{(\rho\beta)_{bf}}+(1-\chi)\right)\theta, \tag{15}$$

$$\frac{\partial p}{\partial y}=0, \tag{16}$$

$$\left(4.97\chi^2+2.72\chi+1\right)\frac{\partial^2\theta}{\partial y^2}+\mathrm{Pr}_{bf}\left(82.1\chi^2+3.9\chi+1\right)\left(1+\frac{3(\sigma-1)\chi}{\sigma+2-(\sigma-1)\chi}\right)\gamma=0. \tag{17}$$

Case (ii) $\left(\gamma Al_2O_3 - C_2H_6O_2\right)$ ***nanofluid***

$$\frac{\partial u}{\partial x}+\frac{\partial v}{\partial y}=0, \tag{18}$$

$$\frac{\partial p}{\partial x}=\frac{\left(306\chi^2-0.19\chi+1\right)}{1+\lambda_1}\frac{\partial^2 u}{\partial y^2}-H^2\left(1+\frac{3(\sigma-1)\chi}{\sigma+2-(\sigma-1)\chi}\right)u+U_{HS}\frac{\partial^2\Phi}{\partial y^2} + Gr\left(\chi\frac{(\rho\beta)_s}{(\rho\beta)_{bf}}+(1-\chi)\right)\theta, \tag{19}$$

$$\frac{\partial p}{\partial y}=0, \tag{20}$$

$$\left(28.905\chi^2+2.8273\chi+1\right)\frac{\partial^2\theta}{\partial y^2}+\mathrm{Pr}_{bf}\left(254.3\chi^2-3\chi+1\right)\left(1+\frac{3(\sigma-1)\chi}{\sigma+2-(\sigma-1)\chi}\right)\gamma=0. \tag{21}$$

Here Re, δ, p, H, U_{HS}, Gr, θ, γ and κ designate the Reynolds number, peristaltic wave number, dimensionless pressure, Hartmann (magnetic body force) number, Helmholtz-Smoluchowski

velocity, thermal Grashof number, nanoparticle temperature, Joule-heating parameter and electroosmosis parameter, respectively.

The relevant dimensionless boundary conditions are specified as follows:

$$\left(\frac{\partial u}{\partial y}\right)_{y=0} = 0,\ u\big|_{y=h} = 0,\ v\big|_{y=0} = 0, v\big|_{y=h} = \frac{\partial h}{\partial t}, \theta\big|_{y=0} = 0, \theta\big|_{y=h} = 1,\ \left.\frac{\partial \Phi}{\partial y}\right|_{y=0} = 0,\ \Phi\big|_{y=h} = 1. \tag{22}$$

4. ANALYTICAL SOLUTIONS

With the Debye-Hückel linearization approximation in Eqn. (13), (i.e. $\sinh \Phi \approx \Phi$) and imposing the boundary conditions defined in Eqn. (22), the electrical potential function is computed as:

$$\Phi = \frac{\cosh(\kappa y)}{\cosh(\kappa h)}. \tag{23}$$

Case (i) $\left(\gamma Al_2O_3 - H_2O\right)$ ***nanofluid***

The analytical solution for the *nanoparticle temperature distribution* is obtained by using Eqn. (17) with corresponding boundary conditions defined in Eqn. (22):

$$\begin{aligned}\theta(y) = \frac{y}{2h}&\left(\frac{\mathrm{Pr}_{bf}\,\gamma h^2}{\left(4.97\chi^2 + 2.72\chi + 1\right)}\left(\frac{3\chi(\sigma-1)}{\sigma - \chi(\sigma-1) + 2}\right)\left(82.1\chi^2 + 3.9\chi + 1\right) + 2\right)\\ &- \frac{\mathrm{Pr}_{bf}\,\gamma y^2}{\left(4.97\chi^2 + 2.72\chi + 1\right)}\left(\frac{3\chi(\sigma-1)}{\sigma - \chi(\sigma-1) + 2}\right)\left(82.1\chi^2 + 3.9\chi + 1\right).\end{aligned} \tag{24}$$

Axial velocity is derived as:

$$\begin{aligned}u(y) = \cosh(a_{10}y)&\left(\frac{\partial p/\partial x}{a_9 a_{10}^2\cosh(a_{10}h)} - \frac{a_{13}\cosh(\kappa h)}{\cosh(a_{10}h)\left(a_{10}^2 - \kappa^2\right)} + \frac{\mathrm{Pr}_{bf}\,a_{11}a_{12}}{a_{10}^4\cosh(a_{10}h)}\right.\\ &\left. - \frac{a_{13}a_{15}h}{a_{10}^2\cosh(a_{10}h)} + \frac{a_{13}a_{15}\sinh(a_{10}h)}{a_{10}^3\cosh(a_{10}h)} + \frac{\mathrm{Pr}_{bf}\,a_{11}a_{12}h^2}{2a_{10}^2\cosh(a_{10}h)}\right)\\ &+ \frac{a_{13}\cosh(\kappa y)}{\left(a_{10}^2 - \kappa^2\right)} - \frac{\partial p/\partial x}{a_9 a_{10}^2} - \frac{\mathrm{Pr}_{bf}\,a_{11}a_{12}}{a_{10}^4} + \frac{a_{13}a_{15}y}{a_{10}^2} - \frac{a_{13}a_{15}\sinh(a_{10}y)}{a_{10}^3} - \frac{\mathrm{Pr}_{bf}\,a_{11}a_{12}y^2}{2a_{10}^2}.\end{aligned} \tag{25}$$

Transverse velocity is derived as:

$$
\begin{aligned}
v(y) = {} & \frac{\partial^2 p}{\partial^2 x}\frac{y}{a_9 a_{10}^2} - \frac{U_{HS}\kappa^2\left(\partial h/\partial x\right)}{a_9\cosh^2(\kappa h)}\frac{\sinh(\kappa h)}{\left(a_{10}^2-\kappa^2\right)} - \left(\frac{-1}{h^2}+\mathrm{Pr}_{bf}\,a_{12}h\right)\frac{\partial h}{\partial x}\frac{a_{11}y^2}{2a_{10}^2} \\
& - \frac{\sinh(a_{10}y)}{a_{10}}\frac{\partial h}{\partial x}\left(\frac{1}{a_9 a_{10}^2\cosh^2(a_{10}h)}\left(\cosh(a_{10}h)\frac{\partial^2 p}{\partial x^2}\frac{\partial x}{\partial h} - \frac{\partial p}{\partial x}\sinh(a_{10}h)a_{10}\right)\right. \\
& + \frac{a_{13}\sinh\left((a_{10}-\kappa)h\right)}{\left(a_{10}^2-\kappa^2\right)\cosh^2(a_{10}h)} - \frac{a_{13}a_{15}}{a_{10}^2\cosh^2(a_{10}h)}\left(\cosh(a_{10}h)-h\sinh(a_{10}h)\right) \\
& - \frac{\mathrm{Pr}_{bf}\,a_{11}a_{12}}{a_{10}^3\cosh^2(a_{10}h)}\sinh(a_{10}h) + \frac{\mathrm{Pr}_{bf}\,a_{11}a_{12}}{2a_{10}^2\cosh^2(a_{10}h)}\left(2h\cosh(a_{10}h)-h^2a_{10}\sinh(a_{10}h)\right) \\
& \left. + \frac{a_3}{a_{10}^2\cosh^2(a_{10}h)}\left(\frac{1}{h}+\frac{\mathrm{Pr}_{bf}\,a_{12}h^2}{2}\right) + \frac{\sinh(a_{10}h)a_{11}}{\cosh(a_{10}h)a_{10}^3}\left(\frac{1}{h^2}-\mathrm{Pr}_{bf}\,a_{12}h\right)\right) \\
& + \frac{a_{11}}{a_{10}^3}\left(\mathrm{Pr}_{bf}\,a_{12}h-\frac{1}{h^2}\right)\frac{\partial h}{\partial x}\frac{\left(\cosh(a_{10}y)-1\right)}{a_{10}},
\end{aligned}
\tag{26}
$$

Axial pressure gradient is derived as:

$$
\begin{aligned}
\frac{\partial p}{\partial x} = {} & -\left(Q - \frac{a_{13}a_{15}h^2}{2a_{10}^2} - \frac{a_4\sinh(\kappa h)}{\kappa\left(a_{10}^2-\kappa^2\right)} + \frac{2a_{13}a_{15}\sinh^2(a_{10}h/2)}{a_{10}^4} + \frac{\mathrm{Pr}_{bf}\,a_{11}a_{12}h}{6a_{10}^4}\left(6+h^2a_{10}^2\right)\right. \\
& - \frac{a_{13}a_{15}\sinh^2(a_{10}h)}{a_2^4\cosh(a_{10}h)} + \frac{a_{13}\cosh(\kappa h)\sinh(a_{10}h)}{a_{10}\cosh(a_{10}h)\left(a_{10}^2-\kappa^2\right)} - \frac{\mathrm{Pr}_{bf}\,a_{11}a_{12}\sinh(a_{10}h)}{a_{10}^5\cosh(a_{10}h)} \\
& \left. + \frac{a_{13}a_{15}h\sinh(a_{10}h)}{a_{10}^3\cosh(a_{10}h)} - \frac{\mathrm{Pr}_{bf}\,a_{11}a_{12}h^2\sinh(a_{10}h)}{2a_{10}^3\cosh(a_{10}h)}\right) \Bigg/ \left(\frac{h}{a_9a_{10}^2} - \frac{\sinh(a_{10}h)}{a_9a_{10}^3\cosh(a_{10}h)}\right)
\end{aligned}
\tag{27}
$$

Introducing the well-known definition of the stream function i.e. the Cauchy-Riemann equations, $u = \frac{\partial\psi}{\partial y}, v = -\frac{\partial\psi}{\partial x}$, *the solution for the stream function* is derived as:

$$\psi(y)=\sinh(a_{10}y)\left(\begin{array}{l}\dfrac{\partial p/\partial x}{a_9a_{10}^3\cosh(a_{10}h)}-\dfrac{a_{13}\cosh(\kappa h)}{a_{10}\cosh(a_{10}h)\left(a_{10}^2-\kappa^2\right)}+\dfrac{\mathrm{Pr}_{bf}\,a_{11}a_{12}}{a_{10}^5\cosh(a_{10}h)}\\ -\dfrac{a_{13}a_{15}h}{a_{10}^3\cosh(a_{10}h)}+\dfrac{a_{13}a_{15}\sinh(a_{10}h)}{a_{10}^4\cosh(a_{10}h)}+\dfrac{\mathrm{Pr}_{bf}\,a_{11}a_{12}h^2}{2a_{10}^3\cosh(a_{10}h)}\end{array}\right)$$
$$+\frac{a_{13}a_{15}y^2}{2a_{10}^2}+\frac{a_{13}\sinh(\kappa y)}{\kappa\left(a_{10}^2-\kappa^2\right)}-\left(\frac{\left(\partial p/\partial x\right)}{a_9a_{10}^2}+\frac{\mathrm{Pr}_{bf}\,a_{11}a_{12}}{a_{10}^4}\right)y \tag{28}$$
$$-\frac{a_{13}a_{15}\left(\cosh(a_{10}y)-1\right)}{a_{10}^4}-\frac{\mathrm{Pr}_{bf}\,a_{11}a_{12}y^3}{6a_{10}^2}.$$

Case (ii) $\left(\gamma Al_2O_3-C_2H_6O_2\right)$ ***nanofluid***

The analytical solution for *nanoparticle temperature distribution* is obtained by using Eqn. (21) with corresponding boundary conditions defined in Eqn. (22):

$$\theta(y)=\frac{y}{2h}\left(\begin{array}{l}\dfrac{\mathrm{Pr}_{bf}\,\gamma h^2}{\left(28.905\chi^2+2.8273\chi+1\right)}\left(\dfrac{3\chi(\sigma-1)}{\sigma-\chi(\sigma-1)+2}\right)\left(254.3\chi^2-3\chi+1\right)+2\\ -\dfrac{\mathrm{Pr}_{bf}\,\gamma y^2}{\left(28.905\chi^2+2.8273\chi+1\right)}\left(\dfrac{3\chi(\sigma-1)}{\sigma-\chi(\sigma-1)+2}\right)\left(254.3\chi^2-3\chi+1\right).\end{array}\right) \tag{29}$$

Axial velocity is derived as:

$$u(y)=\cosh(a_2y)\left(\begin{array}{l}\dfrac{\partial p/\partial x}{a_1a_2^2\cosh(a_2h)}-\dfrac{a_4\cosh(\kappa h)}{\cosh(a_2h)\left(a_2^2-\kappa^2\right)}+\dfrac{\mathrm{Pr}_{bf}\,a_3a_5}{a_2^4\cosh(a_2h)}\\ -\dfrac{a_4a_7h}{a_2^2\cosh(a_2h)}+\dfrac{a_4a_7\sinh(a_2h)}{a_2^3\cosh(a_2h)}+\dfrac{\mathrm{Pr}_{bf}\,a_3a_5h^2}{2a_2^2\cosh(a_2h)}\end{array}\right) \tag{30}$$
$$+\frac{a_4\cosh(\kappa y)}{\left(a_2^2-\kappa^2\right)}-\frac{\partial p/\partial x}{a_1a_2^2}-\frac{\mathrm{Pr}_{bf}\,a_3a_5}{a_2^4}+\frac{a_4a_7y}{a_2^2}-\frac{a_4a_7\sinh(a_2y)}{a_2^3}-\frac{\mathrm{Pr}_{bf}\,a_3a_5y^2}{2a_2^2}.$$

Transverse velocity is derived as:

$$
\begin{aligned}
v(y) = {} & \frac{\partial^2 p}{\partial^2 x}\frac{y}{a_1 a_2^2} - \frac{U_{HS}\kappa^2\left(\partial h/\partial x\right)}{a_1\cosh^2(\kappa h)}\frac{\sinh(\kappa h)}{\left(a_2^2-\kappa^2\right)} - \left(\frac{-1}{h^2}+\mathrm{Pr}_{bf}\,a_5 h\right)\frac{\partial h}{\partial x}\frac{a_3 y^2}{2a_2^2} - \frac{\sinh(a_2 y)}{a_2}\frac{\partial h}{\partial x} \\
& \left(\frac{1}{a_1 a_2^2\cosh^2(a_2 h)}\left(\cosh(a_2 h)\frac{\partial^2 p}{\partial x^2}\frac{\partial x}{\partial h} - \frac{\partial p}{\partial x}\sinh(a_2 h)a_2\right) + \frac{a_4\sinh((a_2-\kappa)h)}{\left(a_2^2-\kappa^2\right)\cosh^2(a_2 h)}\right. \\
& -\frac{\mathrm{Pr}_{bf}\,a_3 a_5}{a_2^3\cosh^2(a_2 h)}\sinh(a_2 h) - \frac{a_4 a_7}{a_2^2\cosh^2(a_2 h)}\left(\cosh(a_2 h) - h\sinh(a_2 h)\right) \\
& +\frac{\mathrm{Pr}_{bf}\,a_3 a_5}{2a_2^2\cosh^2(a_2 h)}\left(2h\cosh(a_2 h) - h^2 a_2\sinh(a_2 h)\right) + \frac{a_3}{a_2^2\cosh^2(a_2 h)}\left(\frac{1}{h}+\frac{\mathrm{Pr}_{bf}\,a_5 h^2}{2}\right) \\
& \left.+\frac{\sinh(a_2 h)a_3}{\cosh(a_2 h)a_2^3}\left(\frac{1}{h^2}-\mathrm{Pr}_{bf}\,a_5 h\right)\right) + \frac{a_3}{a_2^3}\left(\mathrm{Pr}_{bf}\,a_5 h - \frac{1}{h^2}\right)\frac{\partial h}{\partial x}\frac{\left(\cosh(a_2 y)-1\right)}{a_2},
\end{aligned}
\tag{31}
$$

Axial pressure gradient is derived as:

$$
\begin{aligned}
\frac{\partial p}{\partial x} = {} & -\left(Q - \frac{a_4 a_7 h^2}{2a_2^2} - \frac{a_4\sinh(\kappa h)}{\kappa\left(a_2^2-\kappa^2\right)} + \frac{2a_4 a_7\sinh^2(a_2 h/2)}{a_2^4} + \frac{\mathrm{Pr}_{bf}\,a_3 a_5 h}{6a_2^4}\left(6+h^2 a_2^2\right)\right. \\
& -\frac{a_4 a_7\sinh^2(a_2 h)}{a_2^4\cosh(a_2 h)} + \frac{a_4\cosh(\kappa h)\sinh(a_2 h)}{a_2\cosh(a_2 h)\left(a_2^2-\kappa^2\right)} - \frac{\mathrm{Pr}_{bf}\,a_3 a_5\sinh(a_2 h)}{a_2^5\cosh(a_2 h)} \\
& \left.+\frac{a_4 a_7 h\sinh(a_2 h)}{a_2^3\cosh(a_2 h)} - \frac{\mathrm{Pr}_{bf}\,a_3 a_5 h^2\sinh(a_2 h)}{2a_2^3\cosh(a_2 h)}\right) \Bigg/ \left(\frac{h}{a_1 a_2^2} - \frac{\sinh(a_2 h)}{a_1 a_2^3\cosh(a_2 h)}\right)
\end{aligned}
\tag{32}
$$

Stream function is derived as:

$$
\begin{aligned}
\psi(y) = {} & \sinh(a_2 y)\left(\begin{array}{l}\dfrac{\partial p/\partial x}{a_1 a_2^3\cosh(a_2 h)} - \dfrac{a_4\cosh(\kappa h)}{a_2\cosh(a_2 h)\left(a_2^2-\kappa^2\right)} + \dfrac{\mathrm{Pr}_{bf}\,a_3 a_5}{a_2^5\cosh(a_2 h)} \\ -\dfrac{a_4 a_7 h}{a_2^3\cosh(a_2 h)} + \dfrac{a_4 a_7\sinh(a_2 h)}{a_2^4\cosh(a_2 h)} + \dfrac{\mathrm{Pr}_{bf}\,a_3 a_5 h^2}{2a_2^3\cosh(a_2 h)}\end{array}\right) + \frac{a_4 a_7 y^2}{2a_2^2} \\
& +\frac{a_4\sinh(\kappa y)}{\kappa\left(a_2^2-\kappa^2\right)} - \left(\frac{\left(\partial p/\partial x\right)}{a_1 a_2^2} + \frac{\mathrm{Pr}_{bf}\,a_3 a_5}{a_2^4}\right)y - \frac{a_4 a_7\left(\cosh(a_2 y)-1\right)}{a_2^4} - \frac{\mathrm{Pr}_{bf}\,a_3 a_5 y^3}{6a_2^2}.
\end{aligned}
\tag{33}
$$

The constants in the above closed-form solutions are provided in the Appendix.

The *wall shear stress* is defined as:

$$\tau_{xy} = \frac{\mu_{nf}}{\mu_{bf}}\left(\frac{\partial u}{\partial y}\right)_{y\to h} . \tag{34}$$

Heat transfer rate at the microchannel wall can be computed as:

$$Z = \frac{\partial h}{\partial x}\left(\frac{\partial \theta}{\partial y}\right)_{y\to h} . \tag{35}$$

5. NUMERICAL RESULTS AND DISCUSSION

The main focus of this investigation is to study the impact of thermal Grashof number (Gr), Hartmann number (H), electroosmosis parameter (κ), Jeffery (non-Newtonian) parameter (λ_1), solid fractional volume of nanofluid (χ) and Helmholtz-Smoluchowski velocity (U_{HS}) on axial pressure gradient (dp/dx), axial velocity (u) and wall shear stress (τ_{xy}) profiles. To discuss the parametric effects of these selected parameters on $(\gamma Al_2O_3 - \text{water}, \gamma Al_2O_3 - \text{ethylene glycol})$ nanofluids characteristics, **Figs.2-7** are presented and correspond to time $t = 0.4$. These profiles are considered as the single wave propagation model which is mentioned in Eqn. (1).

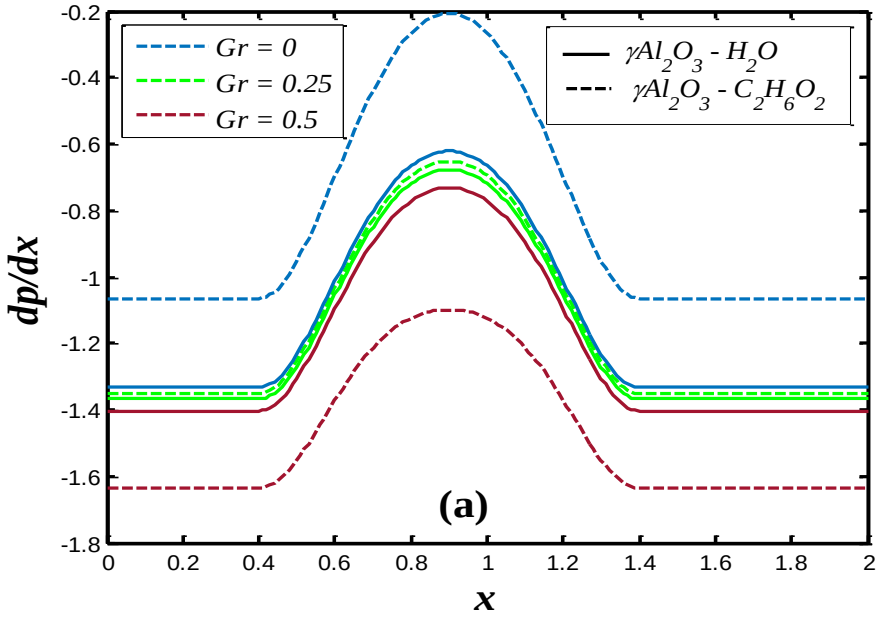

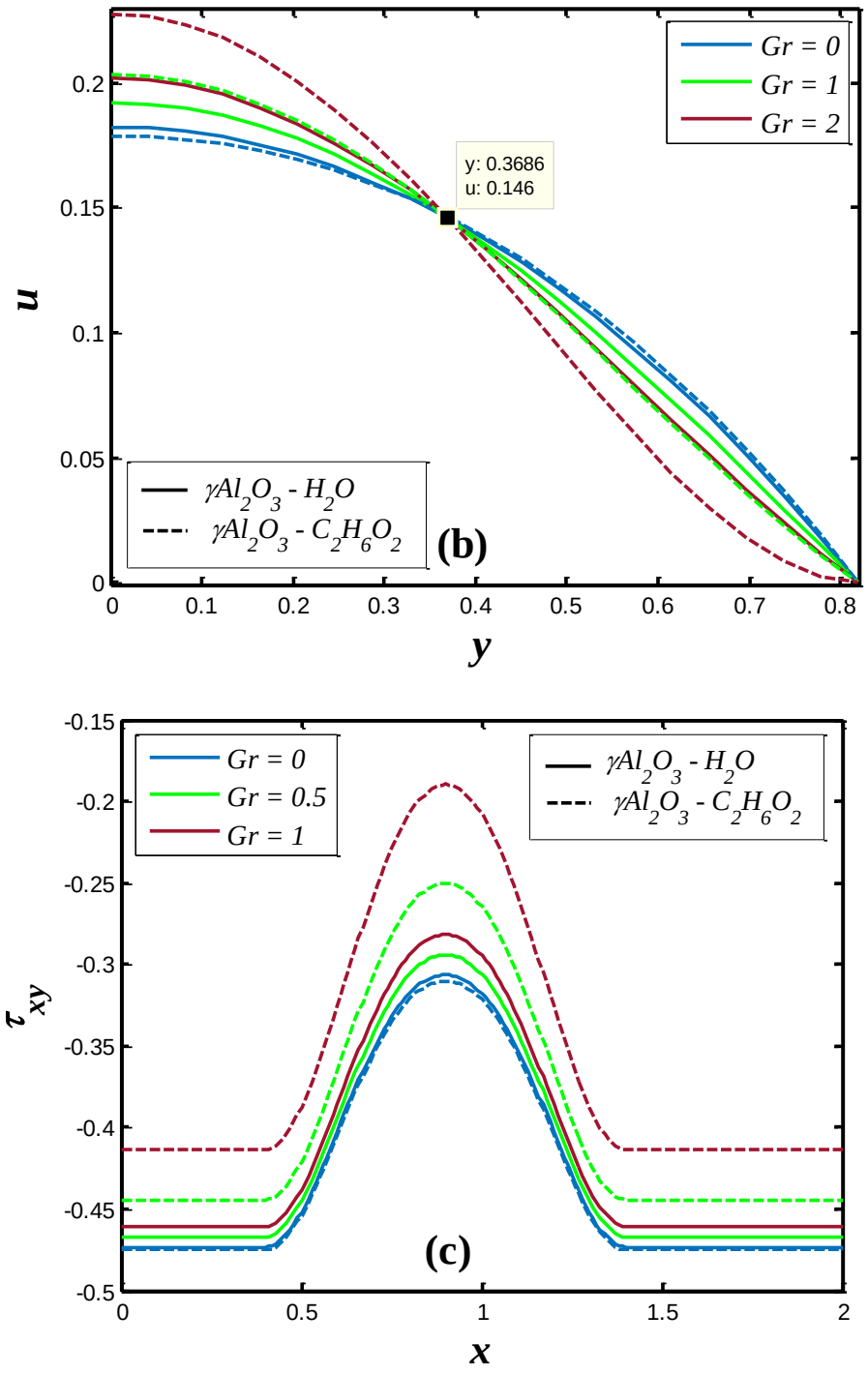

Fig.2: Influence of thermal Grashof number on (a) axial pressure gradient (dp/dx), (b) axial velocity (u) (at $x=0.5$) and (c) axial shear stress (τ_{xy}) for $a=0.2; t=0.4; U_{HS}=2; \kappa=0.2; H=1; \lambda_1=0.2; \chi=0.1; \gamma=0.1$ and $Q=1$.

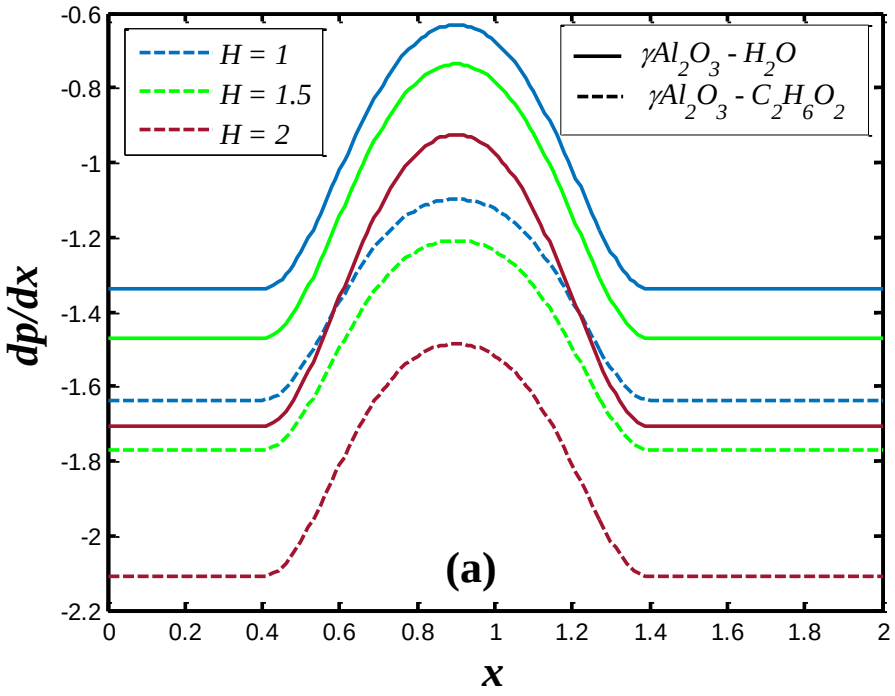
H = 1
H = 1.5
H = 2
γAl2O3 - H2O
γAl2O3 - C2H6O2
dp/dx
x
(a)

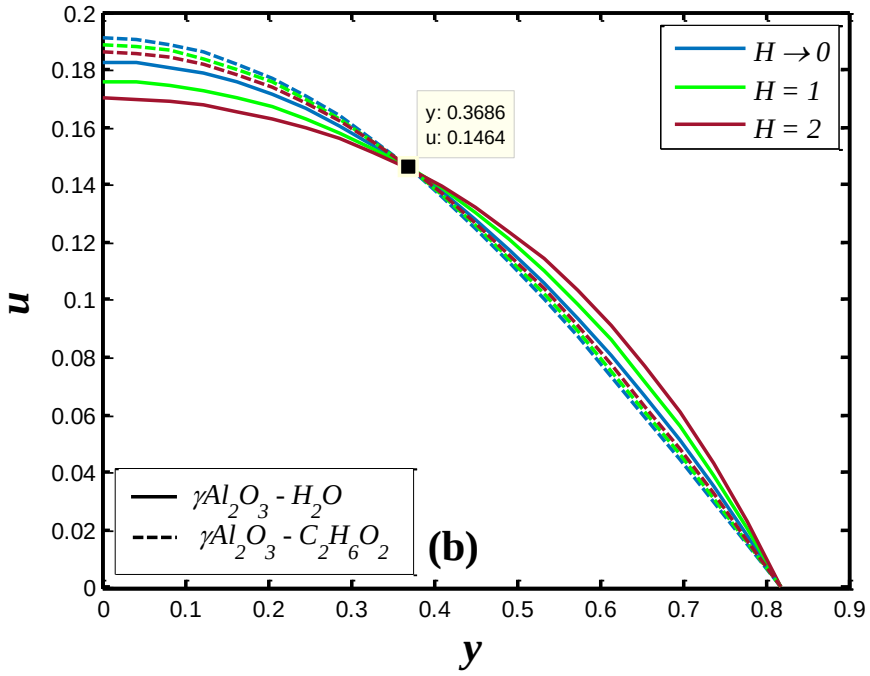
H → 0
H = 1
H = 2
y: 0.3686
u: 0.1464
γAl2O3 - H2O
γAl2O3 - C2H6O2
u
y
(b)

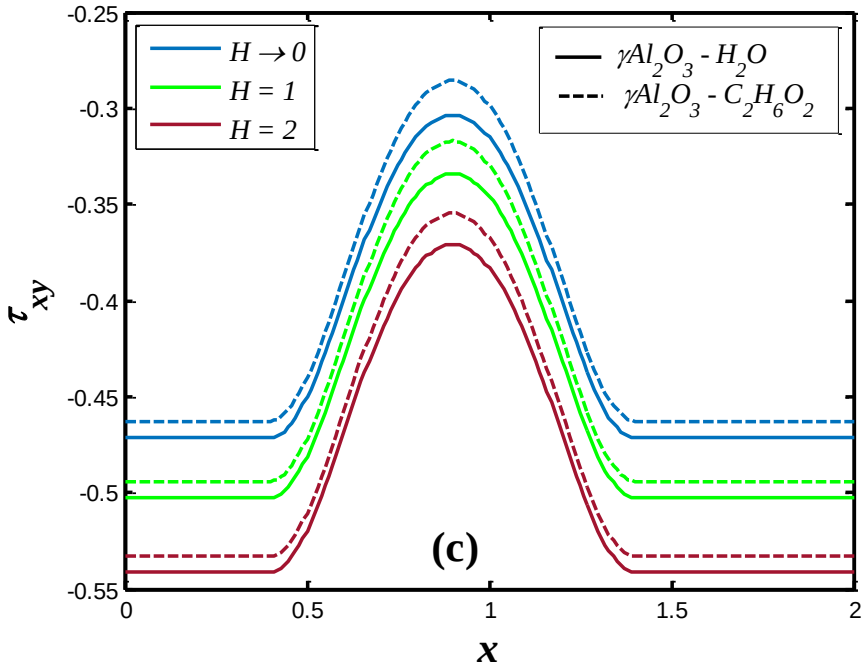

Fig.3 Influence of Hartmann number on (a) axial pressure gradient (dp/dx), (b) axial velocity (u) (at $x=0.5$) and (c) axial shear stress (τ_{xy}) for $a=0.2; t=0.4; U_{HS}=2;\ \kappa=0.2;$ $Gr=0.1;\ \lambda_1=0.2;\ \chi=0.1;\ \gamma=0.1$ and $Q=1$.

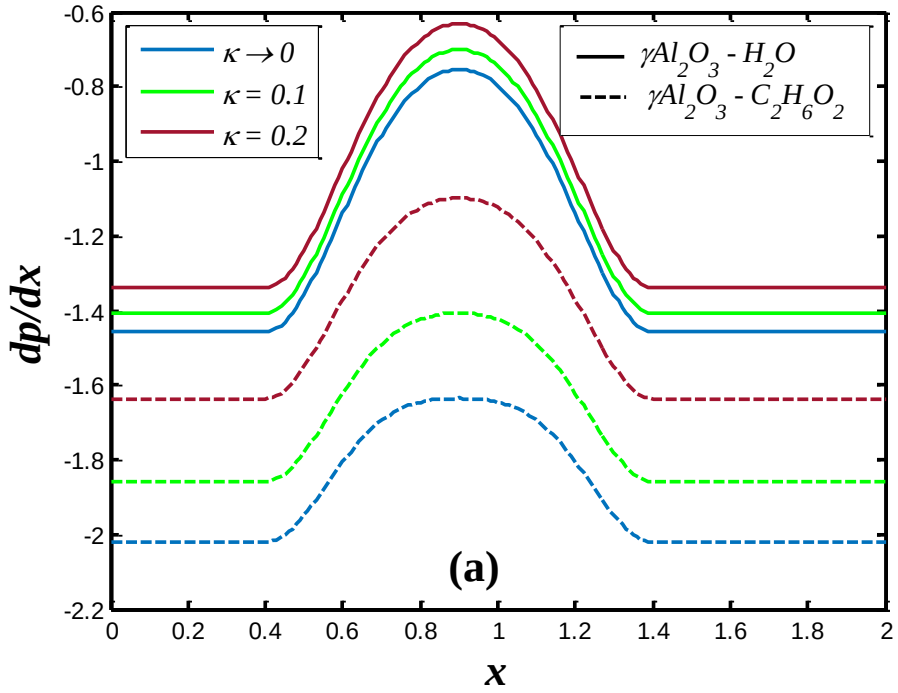

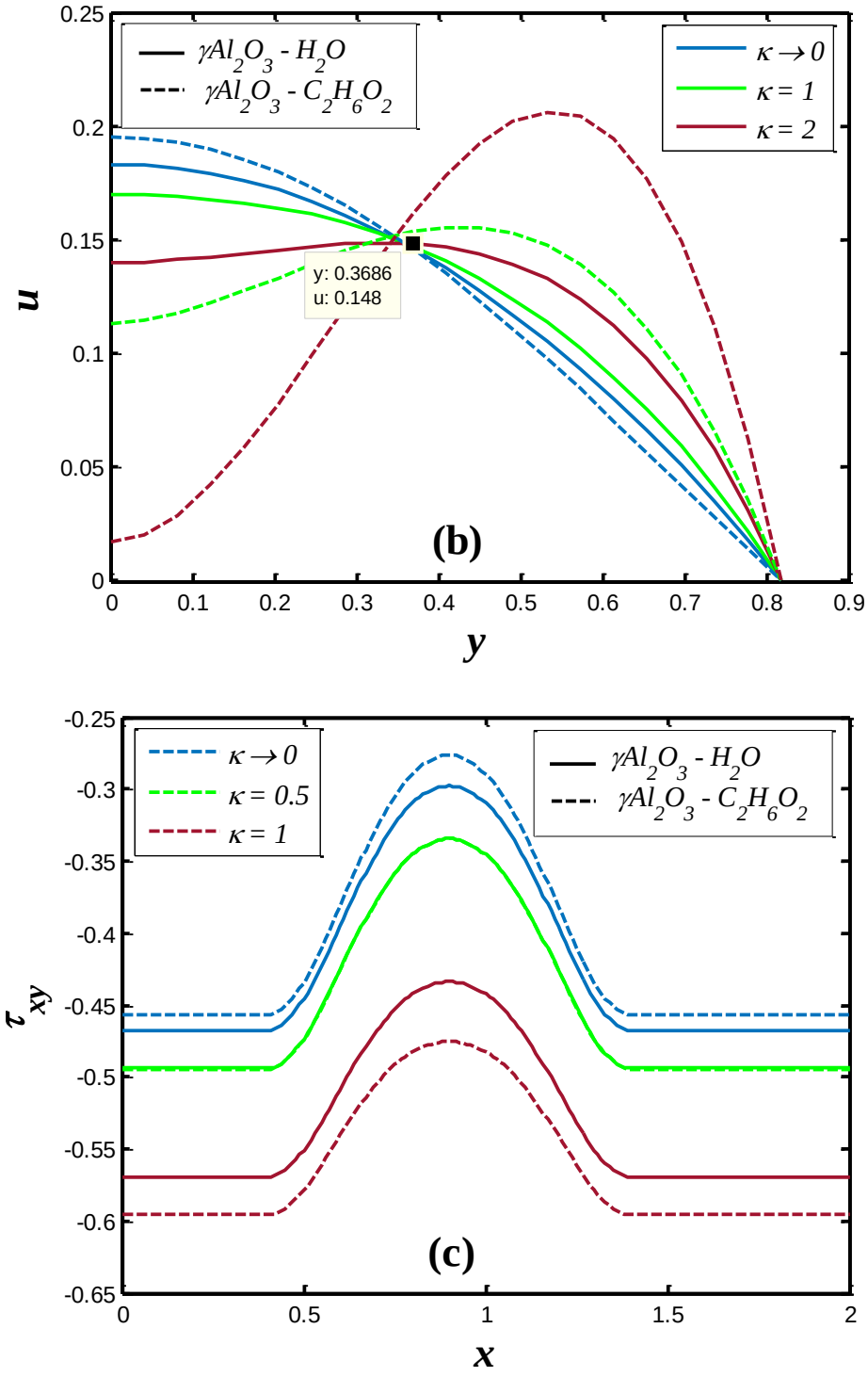

Fig.4 Influence of electroosmosis parameter on (a) axial pressure gradient $\left(dp/dx\right)$, (b) axial velocity $\left(u\right)$ (at $x=0.5$) and (c) axial shear stress $\left(\tau_{xy}\right)$ for $a=0.2; t=0.4; U_{HS}=2;\ H=1;$ $Gr=0.1;\ \lambda_1=0.2;\ \chi=0.1;\ \gamma=0.1$ and $Q=1$.

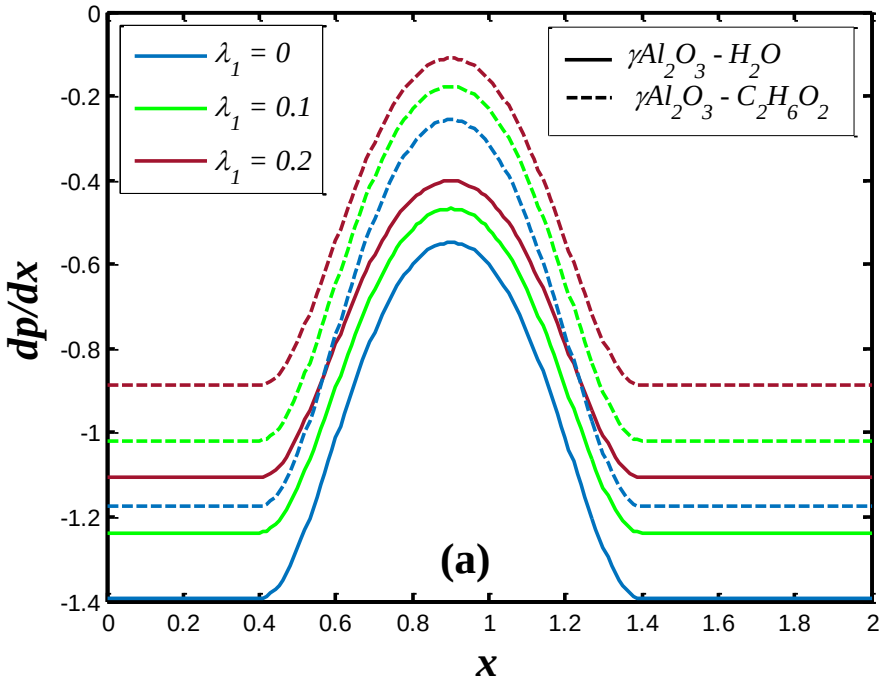
$\lambda_1 = 0$
$\lambda_1 = 0.1$
$\lambda_1 = 0.2$
$\gamma Al_2O_3 - H_2O$
$\gamma Al_2O_3 - C_2H_6O_2$
(a)
dp/dx
x
0
-0.2
-0.4
-0.6
-0.8
-1
-1.2
-1.4
0
0.2
0.4
0.6
0.8
1
1.2
1.4
1.6
1.8
2

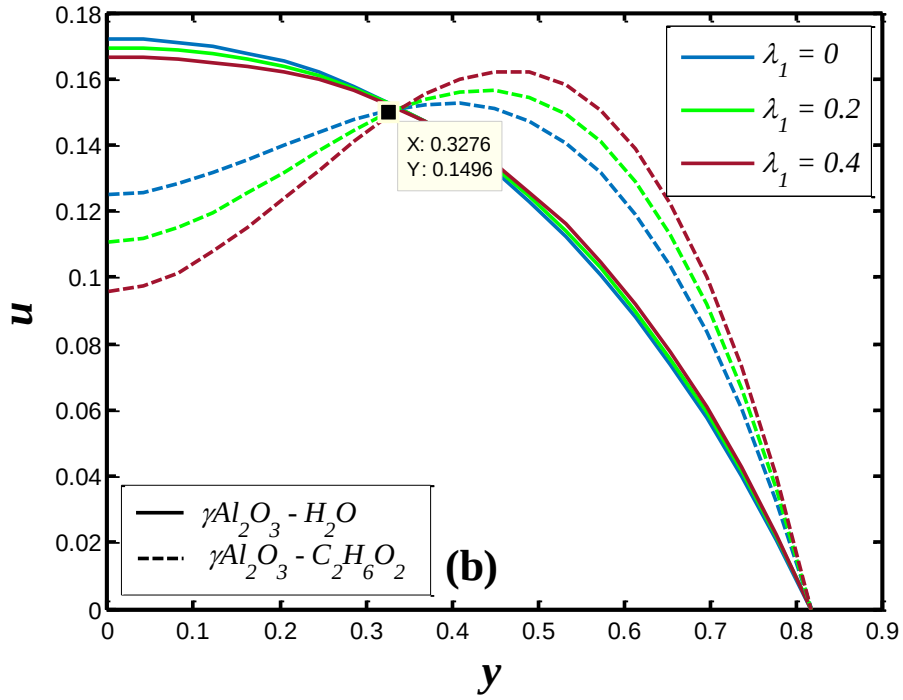
$\lambda_1 = 0$
$\lambda_1 = 0.2$
$\lambda_1 = 0.4$
X: 0.3276
Y: 0.1496
$\gamma Al_2O_3 - H_2O$
$\gamma Al_2O_3 - C_2H_6O_2$
(b)
u
y
0.18
0.16
0.14
0.12
0.1
0.08
0.06
0.04
0.02
0
0
0.1
0.2
0.3
0.4
0.5
0.6
0.7
0.8
0.9

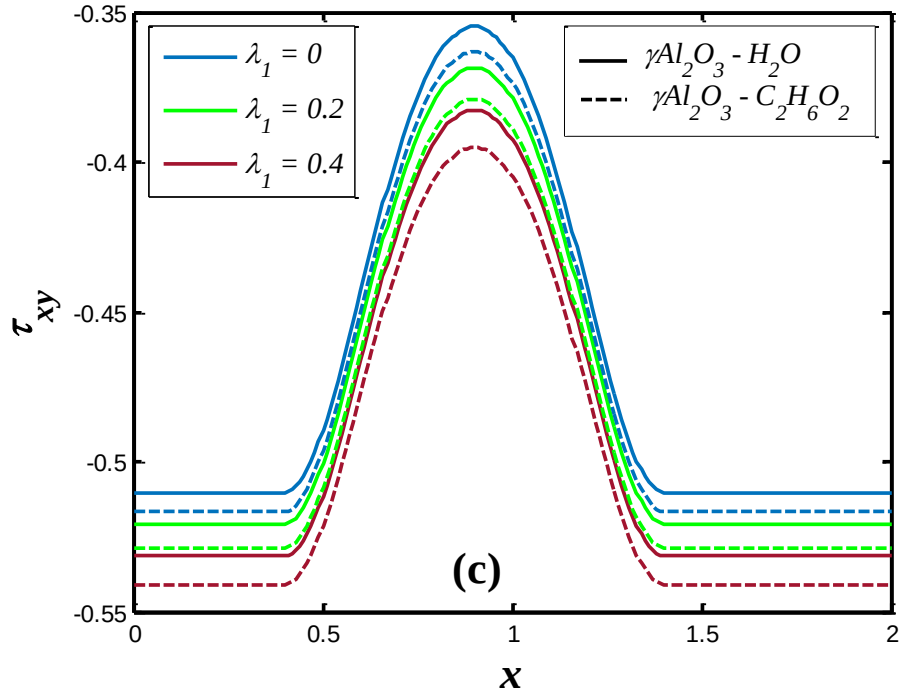

Fig.5 Influence of Jeffery parameter on (a) axial pressure gradient (dp/dx), (b) axial velocity (u) (at $x=0.5$) and (c) axial shear stress (τ_{xy}) for $a = 0.2; t = 0.4; U_{HS} = 2;\ H = 1; Gr = 0.1;$ $\kappa = 1;\ \chi = 0.1;\ \gamma = 0.1$ and $Q = 1$.

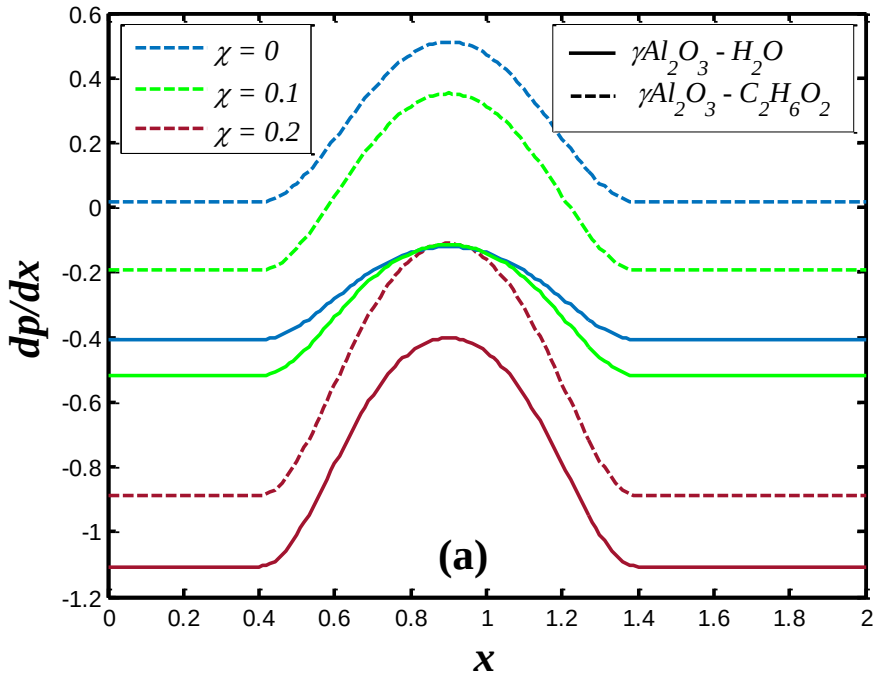

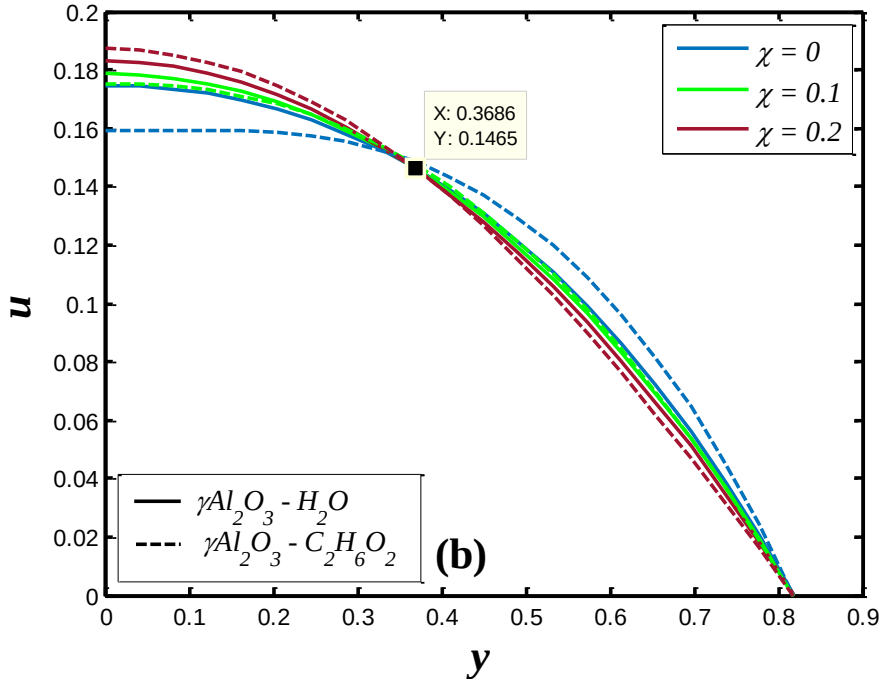

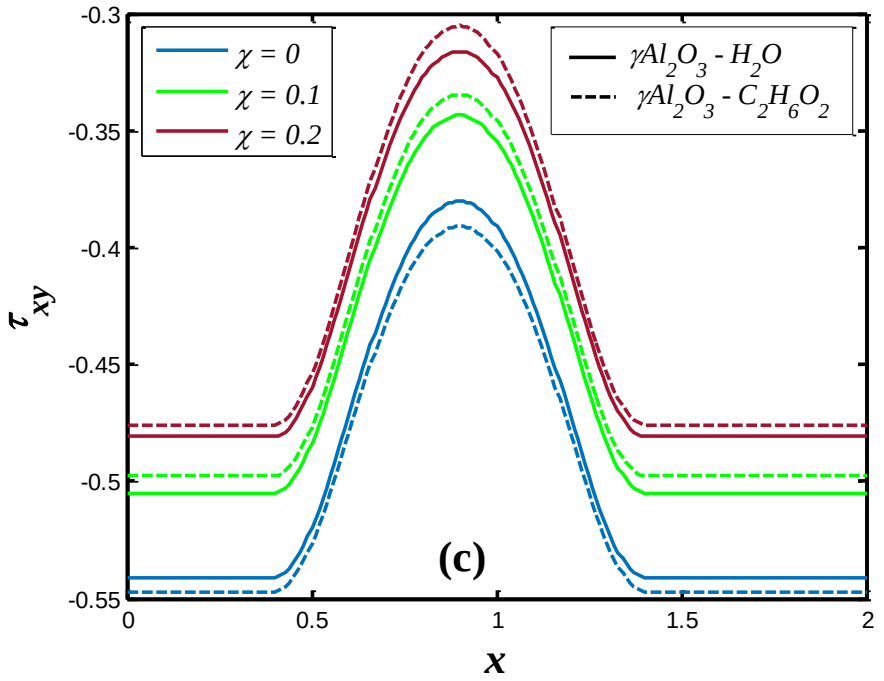

Fig.6 Influence of solid fractional volume of nanofluid on (a) axial pressure gradient (dp/dx), (b) axial velocity (u) (at $x = 0.5$) and (c) axial shear stress (τ_{xy}) for $a = 0.2; t = 0.4; U_{HS} = 1;\ H = 1;\ Gr = 0.1;\ \kappa = 1;\ \lambda_1 = 0.2;\ \gamma = 0.1$ and $Q = 1$.

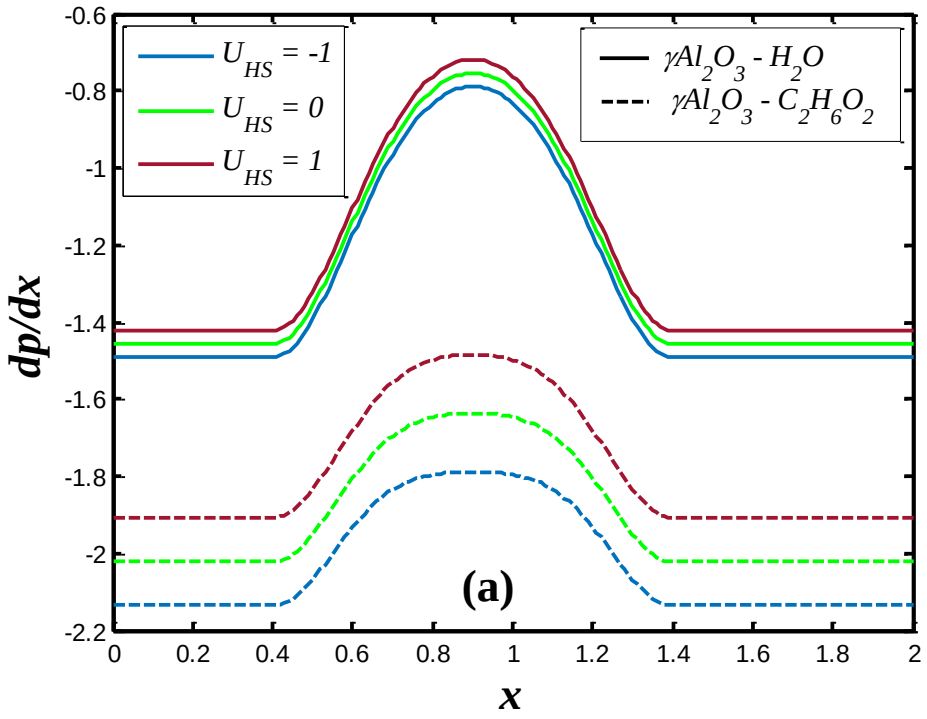
U_{HS} = -1
U_{HS} = 0
U_{HS} = 1
γAl_2O_3 - H_2O
γAl_2O_3 - $C_2H_6O_2$
dp/dx
x
(a)
-0.6
-0.8
-1
-1.2
-1.4
-1.6
-1.8
-2
-2.2
0
0.2
0.4
0.6
0.8
1
1.2
1.4
1.6
1.8
2

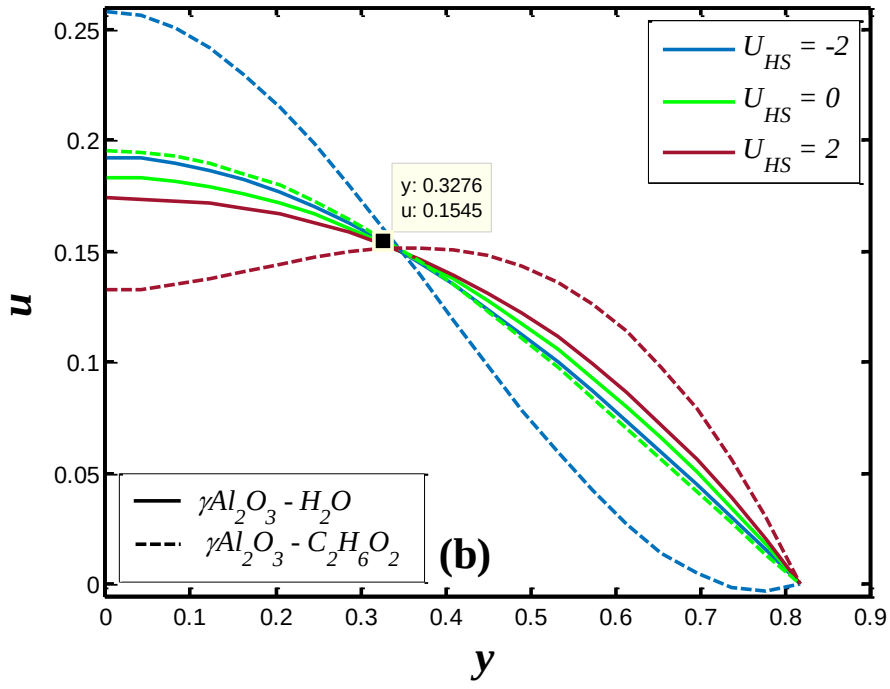
U_{HS} = -2
U_{HS} = 0
U_{HS} = 2
y: 0.3276
u: 0.1545
γAl_2O_3 - H_2O
γAl_2O_3 - $C_2H_6O_2$
(b)
u
y
0.25
0.2
0.15
0.1
0.05
0
0
0.1
0.2
0.3
0.4
0.5
0.6
0.7
0.8
0.9

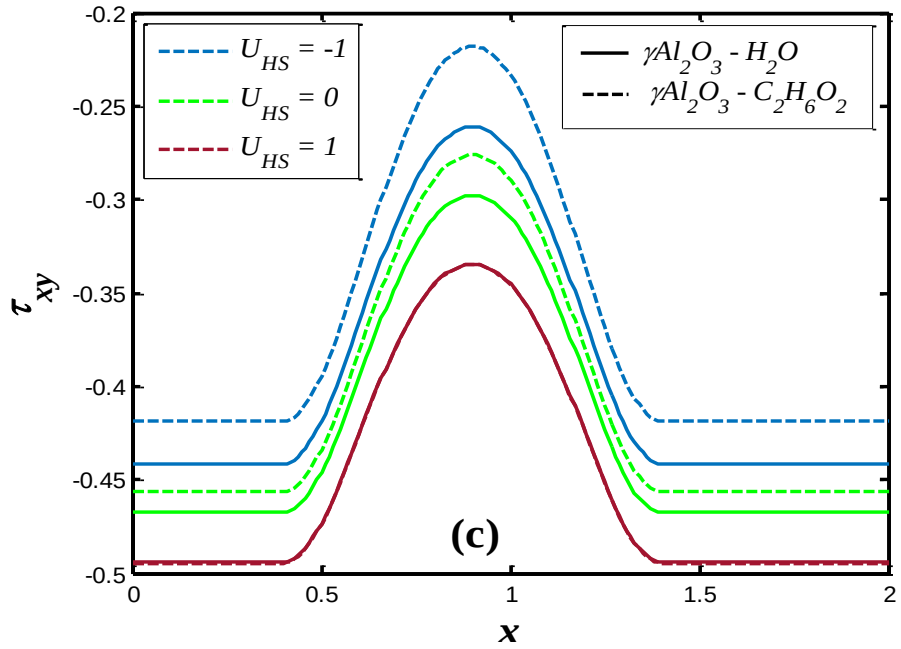

Fig.7 Influence of Helmholtz-Smoluchowski velocity on (a) axial pressure gradient (dp/dx), (b) axial velocity (u) (at $x=0.5$) and (c) axial shear stress (τ_{xy}) for $a=0.2; t=0.4; \chi=0.1; H=1; Gr=0.1; \kappa=1; \lambda_1=0.2; \gamma=0.1$ and $Q=1$.

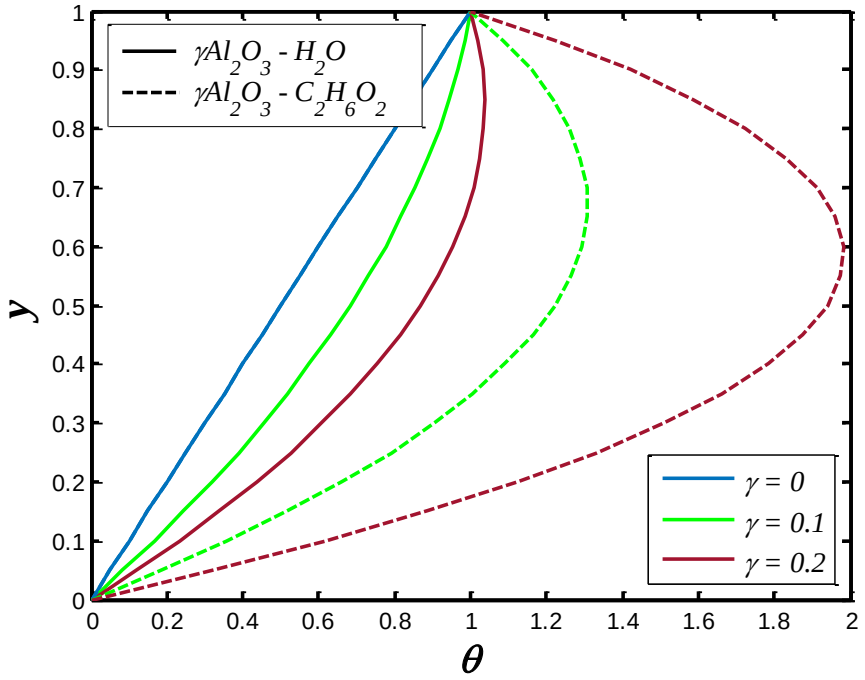

Fig.8 Influence of Joule heating parameter on temperature distribution (θ) for $a=0.1; x=0.6; t=0.1$ and $\chi=0.2$.

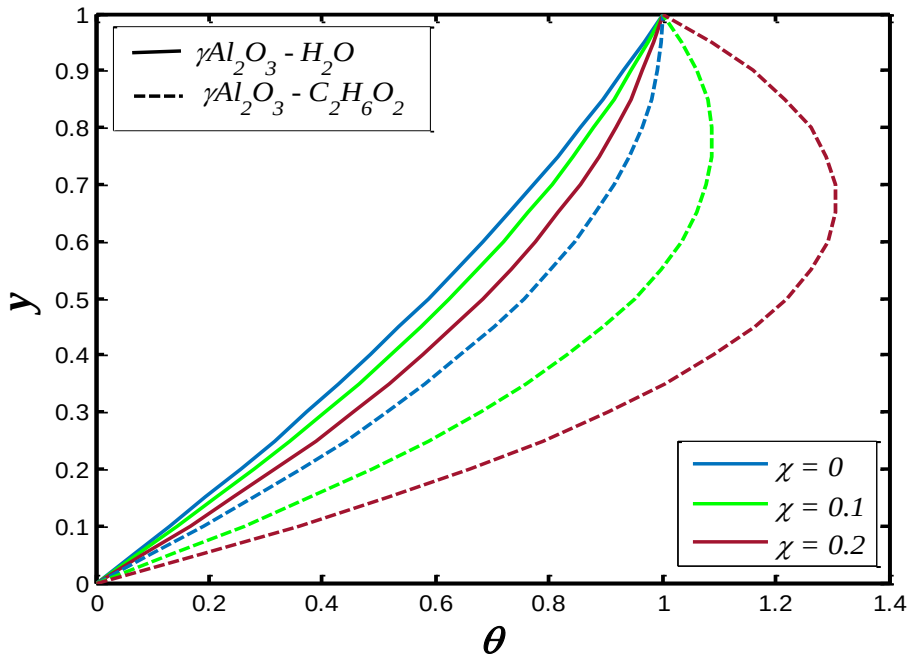

Fig. 9 Influence of solid fractional volume of nanofluid on temperature distribution (θ) for $a = 0.1$; $x = 0.6$; $t = 0.1$ and $\gamma = 0.1$.

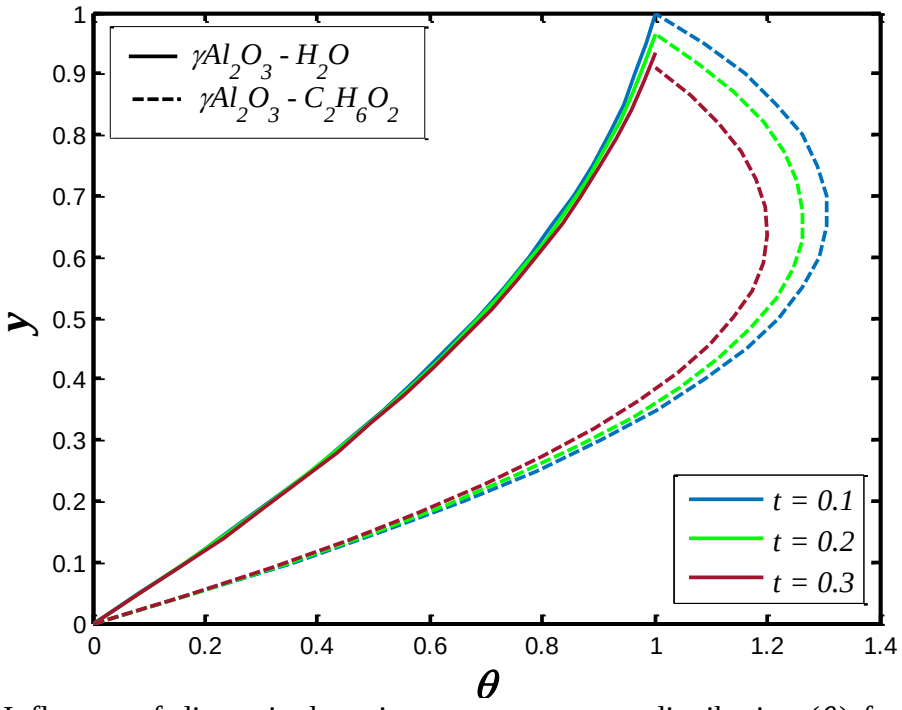

Fig.10 Influence of dimensionless time on temperature distribution (θ) for $a = 0.1$; $x = 0.6$; $\chi = 0.2$ and $\gamma = 0.1$.

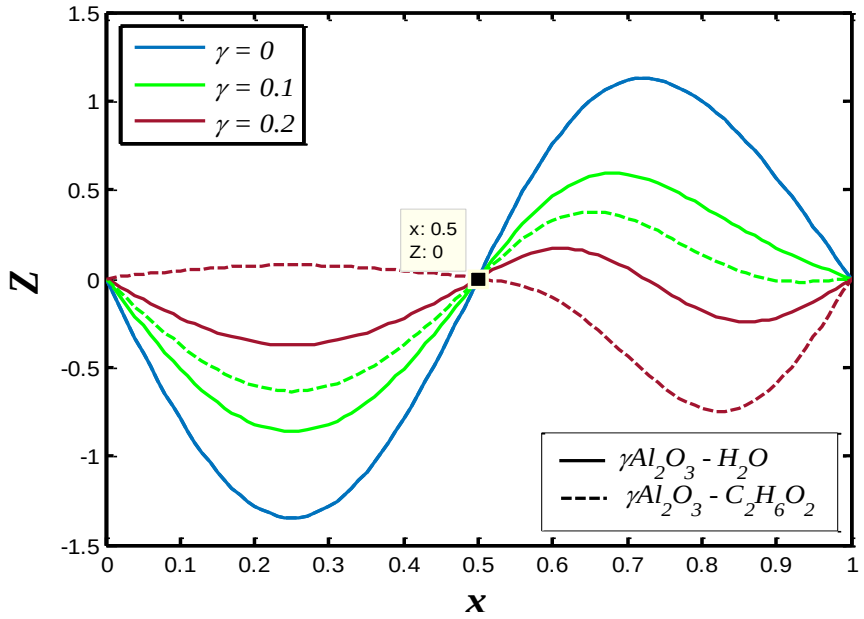

Fig.11 Influence of Joule heating parameter on heat transfer coefficient (***Z***) for $a = 0.3; t = 0.5$ and $\chi = 0.2$.

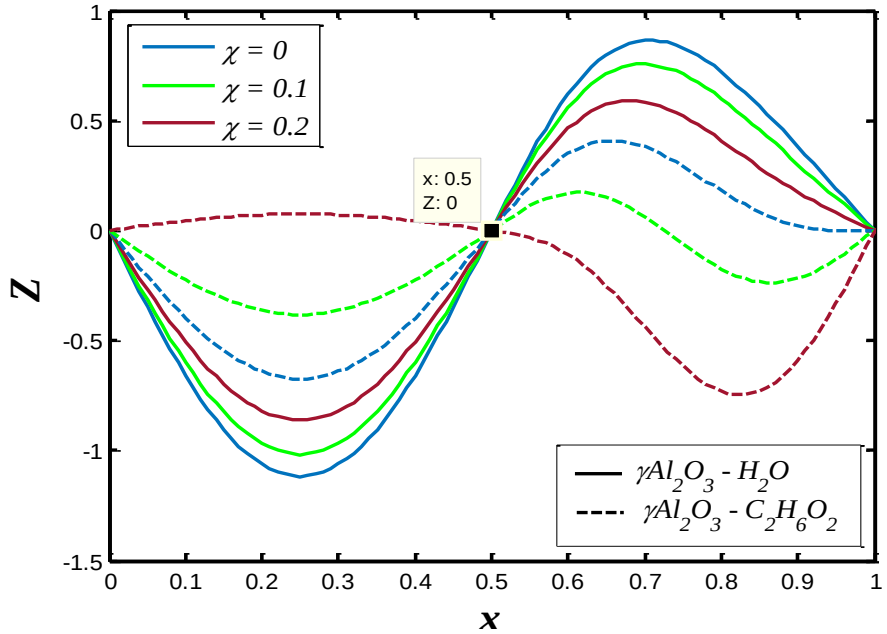

Fig.12 Influence of solid fractional volume of nanofluid on heat transfer coefficient (***Z***) for $a = 0.3; t = 0.5$ and $\gamma = 0.1$.

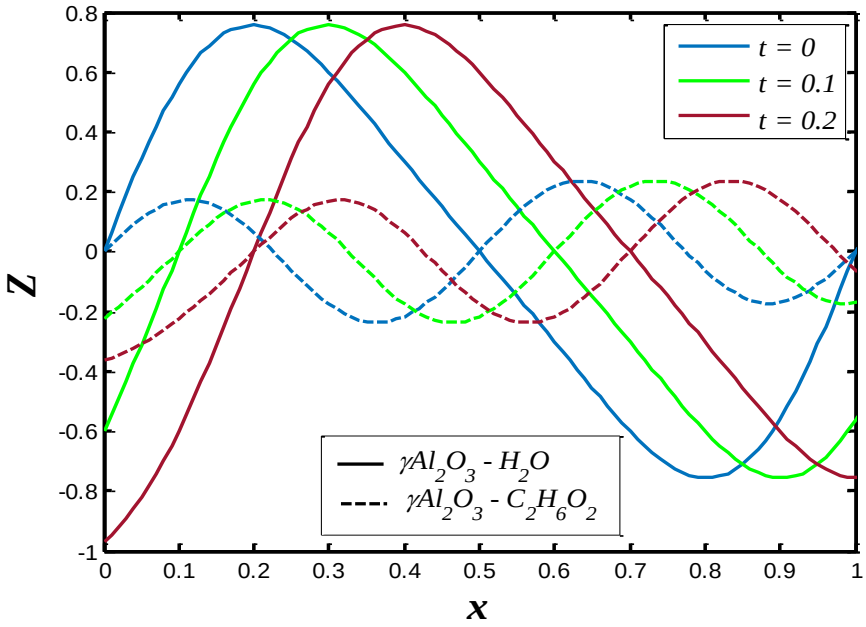

Fig.13 Influence of dimensionless time on heat transfer coefficient (***Z***) for $a = 0.3$; $\chi = 0.5$ and $\gamma = 0.1$.

The effects of thermal Grashof number on axial pressure gradient (dp/dx), axial velocity (u) and wall shear stress (τ_{xy}) profiles are presented in **Figs.2(a-c).** In these plots the default data ; $U_{HS} = 2$; $\kappa = 0.2$; corresponds to practical electro-osmotic microchannel flows – see Jiménez *et al*., [105]. Furthermore, we set $H = B_0 d\sqrt{\frac{\sigma_{bf}}{\mu_{bf}}} = 1$ (magnetic Lorentz force equals the viscous force) – see Duwairi and Abdullah [38]. Additionally 10% nanoparticle doping is prescribed, following Das *et al.* [6] and relatively weak electrical field is imposed, $\gamma = \frac{\sigma_{bf} d^2 E_x^2}{\kappa_{bf}(T_1 - T_0)} = 0.1$. Weak viscoelastic effect is also considered which is more amenable for higher mobility working fluids i.e. $\lambda_1 = 0.2$, for which relaxation time is much smaller than the retardation time, as noted by Bird *et al*. [106].

Fig.2(a) indicates that with enhancement in the magnitude of thermal Grashof number (Gr) there is a suppression in axial pressure gradient. Thermal Grashof number as defined in Eqn. (12) i.e. $Gr = \frac{g(\rho\beta)_f (T_1 - T_0) d^2}{c\mu_{bf}}$ embodies the relative contribution of *thermal buoyancy force to viscous*

hydrodynamic force. It is known to accelerate the flow, as demonstrated experimentally by Gebhart *et al.* [107], and via the continuity principle, this manifests in a simultaneous reduction in pressure in the electromagnetic peristaltic nanofluid regime i.e. stronger thermal buoyancy depletes the axial pressure gradient. Thermal effects therefore exert a considerable influence on hydromechanical effects in the pumping dynamics. For $Gr = 0.5$, the pressure gradient is higher in the case of $(\gamma Al_2O_3 - H_2O)$ nanofluid as compared to $(\gamma Al_2O_3 - C_2H_6O_2)$ nanofluid. However, the opposite trends are computed at lower thermal Grashof number i.e. $Gr = 0{,}0.25$. It is noteworthy to mention that for *Gr = 0* thermal buoyancy is negated, and the regime becomes one of *forced convection*, for which the momentum and energy conservation equations are decoupled. For natural convection, *Gr > 0* and evidently there is a significant interplay between pressure gradient and thermal effects with logical implications in microchannel energy systems design. From **Fig.2(b),** it is noticed that the axial velocity increases in the region $(0 \le y \le 0.3686)$ with the enhanced value of thermal Grashof number *i.e. substantial axial flow acceleration is induced;* however there is a reduction in axial velocity in the region $(0.3686 \le y \le 0.82)$ *i.e. flow retardation,* for the $(\gamma Al_2O_3 - H_2O, \gamma Al_2O_3 - C_2H_6O_2)$ nanofluids, and this is attributable to the re-distribution in momentum in the wavy flow regime, as noted by Takabatake *et al.* [80], among many others. For $Gr = 0$, the axial velocity is of marginally higher magnitude for $(\gamma Al_2O_3 - H_2O)$ nanofluid as compared to $(\gamma Al_2O_3 - C_2H_6O_2)$ nanofluid. However with *Gr* = 1.2 (thermal buoyancy > viscous force) in *free convection*, axial velocity is greater for $(\gamma Al_2O_3 - C_2H_6O_2)$ nanofluid as compared to $(\gamma Al_2O_3 - H_2O)$ nanofluid in the region $(0 \le y \le 0.3686)$ and reverse flow patterns are computed in the region $(0.3686 \le y \le 0.82)$. **Fig. 2(c)** depicts the local wall shear stress distribution under the effects of Grashof number for both $(\gamma Al_2O_3 - H_2O)$ and $(\gamma Al_2O_3 - C_2H_6O_2)$ nanofluids. It is evident that the magnitude of wall shear stress increases with greater Grashof number since the axial flow is boosted which manifests in higher shear rates at the microchannel boundaries. In the absence of buoyancy force ($Gr = 0$), shear stress is higher for $(\gamma Al_2O_3 - H_2O)$ nanofluid as compared to $(\gamma Al_2O_3 - C_2H_6O_2)$ nanofluid; however with relatively strong thermal

buoyancy present i.e. *Gr = 1.2*, shear stress for $\left(\gamma Al_2O_3 - C_2H_6O_2\right)$ nanofluid clearly exceeds that for $\left(\gamma Al_2O_3 - H_2O\right)$ nanofluid. The *base fluid viscosity* i.e. ethylene glycol is significantly more viscous than water, which inevitably contributes to the variation in shear stress.

Figs. 3(a-c) visualize the magnetic field effect (Hartmann number) on axial pressure gradient $\left(dp/dx\right)$, axial velocity $\left(u\right)$ and wall shear stress $\left(\tau_{xy}\right)$ profiles for $\left(\gamma Al_2O_3 - H_2O,\ \gamma Al_2O_3 - C_2H_6O_2\right)$ nanofluids. **Fig. 3(a)** reveals that by enhancing Hartmann number *H*, the magnitude of pressure gradient $\left(dp/dx\right)$ decreases. The Hartmann number (*H*) as noted earlier represents the ratio of electromagnetic (Lorentz) force to viscous force; higher *H* indicates stronger Lorentz force which suppresses pressure gradient i.e. greater control is achieved of pressure distribution for *H* = 2 (magnetic force is double the viscous force) compared with *H* = 1 (both forces are equal). **Fig. 3(b)** shows that with increment in Hartmann number, the axial velocity of $\left(\gamma Al_2O_3 - water,\ \gamma Al_2O_3 - ethylene\ glycol\right)$ nanofluids, decreases for small $y\ \left(0 \le y \le 0.3686\right)$ whereas for large $y\ \left(0.3686 \le y \le 0.82\right)$, axial velocity increases. The switch in behaviour is characteristic of microchannel flows and is attributable to the re-distribution in linear momentum in the regime, as elaborated by Cramer and Pai [108]. However, it is pertinent to note, that *flow reversal is not induced* i.e. negative velocities are not generated anywhere in the regime and this is also a characteristic of peristaltic pumping which avoids the backflow associated with other pumping mechanisms in energy systems. Magnetic retarding force is clearly a potent regulatory mechanism for specific zones in the microchannel regime i.e. it can mobilize both deceleration and acceleration where required and provides engineers with a useful and non-intrusive technique with minimal maintenance for optimizing microchannel performance, as noted by Rosa [35]. **Fig. 3(c)** shows that an increase in the Hartmann number creates a decrement in wall shear stress $\left(\tau_{xy}\right)$ profile in the core section of the wavy channel. Strong axial flow deceleration is therefore generated again due to the inhibiting effect of transverse static magnetic field. At all axial locations, $(\boldsymbol{\gamma Al_2O_3 - C_2H_6O_2})$ nanofluids achieve noticeably higher shear stresses however than $(\boldsymbol{\gamma Al_2O_3 - H_2O})$ nanofluids. The non-magnetic case (*H* = 0) overall achieves the higher shear stresses compared to any magnetohydrodynamic case. Significant flow control is therefore achievable with imposition of transverse magnetic fields. At the entry zone

(low values of *x*), and also exit zone (higher values of *x*) strongly negative shear stress is generated whereas in the central axial zone consistently lower negative shear stresses are computed, for all values of Hartmann number, *H*.

The effects of Debye-Hückel parameter (κ) on axial pressure gradient (dp/dx), axial velocity (u) and wall shear stress (τ_{xy}) profiles for $(\gamma Al_2O_3 - H_2O,\ \gamma Al_2O_3 - C_2H_6O_2)$ nanofluids have been displayed in **Figs.4 (a-c).** The Debye-Hückel parameter κ is the inverse of the Debye length (i.e. electric double layer (EDL) thickness). It is observed from **Fig.4(a),** axial pressure gradient increases at core part of the channel with the enhanced $\boldsymbol{\kappa}$ -value for both $(\gamma Al_2O_3 - H_2O,\ \gamma Al_2O_3 - C_2H_6O_2)$ nanofluids. The case $\kappa \to 0$ corresponds to the *non-electrical* scenario (magnetohydrodynamic viscoelastic nanofluid peristaltic flow, since *H* is prescribed as 1). **Fig. 4 (b)** is perceived that an increasing trend is noticed in the right part region of single wave channel. Conversely, opposite behavior is noted in the left part of the channel region. A decrease in wall shear stress profile is noticed when Debye-Hückel parameter κ is enhanced for both $(\gamma Al_2O_3 - water,\ \gamma Al_2O_3 - ethylene\ glycol)$ nanofluids, which is presented in **Fig. 4 (c)**. It is noticed that the effect of $\gamma Al_2O_3 - C_2H_6O_2$ nanofluid more strongly influences on wall shear stress profile as compared with the $\gamma Al_2O_3 - H_2O$ nanofluid. The axial electric field effectively acts perpendicular to the decay of the EDL (or equivalently parallel with the surface). The surplus of either positive or negative ions results in a net body force on the electromagnetic viscoelastic nanofluid proportional to the local net charge density. The resulting velocity profile comprises a region of quite high shear rates near the surface where the velocity ascends from zero at the shear plane to its bulk phase velocity at the edge of the EDL. The proportionality between bulk phase velocity and the strength of the electric field, E_x, is quantified by the electroosmotic mobility which is dependent on both surface and solution phase properties. Contrary to conventional pressure-driven microchannel systems, uniform electroosmotic flow exhibits a flat or "plug flow" velocity profile outside the double layer region. Overall, it is abundantly evident that the electro-osmotic effect imparts a significant modification in microchannel transport phenomena characteristics.

The impact of Jeffery parameter ($\lambda_1\ i.e.$ non-Newtonian parameter) on axial pressure gradient (dp/dx), axial velocity (u) and wall shear stress (τ_{xy}) profiles for $(\gamma Al_2O_3 - H_2O,\ \gamma Al_2O_3 - C_2H_6O_2)$ nanofluids are illustrated in **Fig.5 (a-c).** From **Fig. 5(a)**, it is noticed that elevation in the Jeffery parameter induces a significant delineation in the development of the axial pressure gradient for both $(\gamma Al_2O_3 - H_2O,\ \gamma Al_2O_3 - C_2H_6O_2)$ nanofluids. It is specified that the axial pressure gradient increases as the base fluids behavior changes from Newtonian $(\lambda_1 = 0)$ to Jeffery nanofluids $(\lambda_1 > 0)$ for both $(\gamma Al_2O_3 - water,\ \gamma Al_2O_3 - ethylene\ glycol)$ nanofluids. In **Fig. 5(b),** the axial velocity profile proportionately reduces in the left part of region $y\ (0 \le y \le 0.3686)$ and the opposite trend is observed in the right part of region $y\ (0.3686 \le y \le 0.82)$ for both $(\gamma Al_2O_3 - H_2O,\ \gamma Al_2O_3 - C_2H_6O_2)$ nanofluids. Also, from **Fig. 5(c),** it is observed that the wall shear stress profile distribution reduces with enhancing the value of Jeffery parameter; wall shear stress attains a maximum value for Newtonian nanofluids as compared to Jeffrey nanofluids. Jeffrey's parameter i.e. $\lambda_1\ i.e$ arises in the denominator of the augmented shear term in the transformed momentum equations e.g. as the term, $\frac{(123\chi^2+7.3\chi+1)}{1+\lambda_1}\frac{\partial^2 u}{\partial y^2}$ in Eqn. (14). In certain zones of the microchannel, an increase in relaxation time relative to retardation time (λ_1>0) produces considerable deceleration (fig. 5b) in the flow since elastic forces begin to dominate the viscous forces and the nanofluid takes longer to return to its relaxed state after deformation. There will also be an associated elevation in pressure difference as a result of this flow deceleration (as seen in fig. 5a). Weakly viscoelastic nanofluid ($\lambda_1 = 0.2$) therefore generates higher axial velocity magnitudes compared with stronger viscoelastic nanofluid ($\lambda_1 = 0.2$) but substantially lower magnitudes than Newtonian nanofluid (λ_1=0 for which relaxation and retardation effects vanish) . It is also of interest that even with *high relaxation: retardation time ratio* the flow is never reversed i.e. *back flow* is not induced as testified to by the consistently positive values of axial velocity in Fig. 5b. the strongly laminar nature of the flow also ensures that flow separation or boundary layer detachment from the walls at the entry zone is also eliminated. Furthermore, there is an upper limit to physically realistic working fluids and therefore the case of λ_1 exceeding unity is not appropriate and ignored, as noted by Bird *et al.* [106].

Figs. 6(a-c) illustrate the effects of solid fractional volume of nanofluid (χ) on $\frac{dp}{dx}$, u and τ_{xy} profiles for both $(\gamma Al_2O_3 - H_2O,\ \gamma Al_2O_3 - C_2H_6O_2)$ nanofluids. **Fig. 6(a)** exposes that a significant drop in the axial pressure gradient of both nanofluids is identified when $(\gamma Al_2O_3 - water,\ \gamma Al_2O_3 - ethylene\ glycol)$ nanofluids are prepared with large solid fractional volume of nanofluid i.e. high percentage doping of the base fluids with nanoparticles. Clearly, this behaviour is generated by the enhanced viscosity of the homogenously dispersed $\gamma Al_2O_3 - ethylene\ glycol$ nanoparticles. **Fig. 6(b)** is drawn to explain the development in the axial velocity profile with an increment in the solid fractional volume of nanofluid; strong flow acceleration is computed in left region $y\ (0 \le y \le 0.3686)$. It is also noticed that the wall shear stress is boosted with an increase in solid fractional volume of nanofluid (χ) as depicted in **Fig.6(c).** The $\gamma Al_2O_3 - ethyleneglycol$ nanofluid is influenced more dramatically with solid fractional volume of nanofluid as compared with $\boldsymbol{\gamma Al_2O_3 - water}$ nanofluid.

The variations in $\frac{dp}{dx}$, u and τ_{xy} for $\gamma Al_2O_3 - water, \gamma Al_2O_3 - ethyleneglycol$ nanofluids with increment in Helmholtz-Smoluchowski velocity (U_{HS}) are examined through **Figs.7(a-c)**. Helmholtz-Smoluchowski velocity (maximum electro-osmotic velocity) represent the effects of external electric field and is defined as $U_{HS} = -\dfrac{\mathbf{E}_x \varepsilon_{ef} \varsigma}{c\mu_{bf}}$. A positive value of $\boldsymbol{U_{HS} > 0}$ implies an opposing electrical field orientation in the negative X-direction, $\boldsymbol{U_{HS} = 0}$ corresponds to an absence of electric field and $\boldsymbol{U_{HS} < 0}$ is associated with an assistive (supportive) electric field in the non-negative X direction. It is apparent that for supporting electric field, axial pressure gradient is minimum whereas it is a maximum for an opposing electric field, as visualized in **Fig. 7(a)** for both nanofluid cases $(\gamma Al_2O_3 - H_2O,\ \gamma Al_2O_3 - C_2H_6O_2)$. From **Fig. 7(b),** the impact of $\boldsymbol{U_{HS}}$ on axial velocity reveals that axial flow acceleration is induced in right section of the region whereas the converse effect arises in the left section of the region. An increase in $\boldsymbol{U_{HS}}$ in the non-positive direction physically infers the presence of a strong assistive axial electric field which produces enhancement in the wall shear stress magnitudes (see **Fig.7(c)**) for both $(\gamma Al_2O_3 - H_2O,\ \gamma Al_2O_3 - C_2H_6O_2)$ nanofluids.

The evolution in temperature distribution with Joule electrothermal parameter (γ), solid fractional volume of nanofluid (χ) and dimensionless time (t) is visualized in **Figs. 8-10.** It is observed that the temperature of $\boldsymbol{\gamma Al_2O_3 - water}$ nanofluid is noticeably less than the temperature computed for $\gamma Al_2O_3 - ethyleneglycol$ nanofluid. These plots for temperature distribution are based on the no-slip boundary conditions enforced on the peristaltic microchannel walls. As a result of the shear thinning nature of $\gamma Al_2O_3 - water$ nanofluid ionic solution and a lower viscosity relative to that of $\gamma Al_2O_3 - ethylene\ glycol$ nanofluid, the momentum diffusion rate of $\gamma Al_2O_3 - water$ nanofluid exceeds that of the $\gamma Al_2O_3 - ethylene\ glycol$ nanofluid (Prandtl number is fixed and expresses the ratio of momentum and thermal diffusivities). Due to *enhanced cooling* within the flow regime, $\boldsymbol{\gamma Al_2O_3 - water}$ nanofluid achieves lower temperature magnitudes than $\gamma Al_2O_3 - ethylene\ glycol$ nanofluid. **Fig. 8** depicts the alteration in the temperature profile of $(\gamma Al_2O_3 - H_2O,\ \gamma Al_2O_3 - C_2H_6O_2)$ nanofluids via higher values Joule heating parameter. The temperature distribution of the nanofluid is improved when more electric energy is changed into thermal energy due to Joule electrical dissipation, which is a very important effect in real electro-osmotic fluid dynamics. A substantial elevation in the $(\gamma Al_2O_3 - H_2O,\ \gamma Al_2O_3 - C_2H_6O_2)$ nanofluids temperature distribution for growing values of the solid fractional volume of nanofluid is also demonstrated in **Fig.9.** As expected, due to the growth in the conductive heat transfer, there is a growth in the temperature distribution of the $(\gamma Al_2O_3 - H_2O,\ \gamma Al_2O_3 - C_2H_6O_2)$ nanofluids for larger solid fractional volume of nanofluid. **Fig. 10** indicates that a considerable enhancement in temperature profile is induced with progress in time. The free movement of $\boldsymbol{\gamma Al_2O_3 - water}$ nanoparticles increases with interaction between molecules and the resulting ballistic collisions which is possible due to lower viscosity. However the $\gamma Al_2O_3 - ethyleneglycol$ nanofluid possesses a higher viscosity and this inhibits ballistic nanoparticle collisions which results in a depression in nanoparticle temperature distribution since interaction between the molecules is inhibited.

Figs.11-13 illustrate the evolution in heat transfer coefficient (***Z***) with selected parameters for both $(\gamma Al_2O_3 - H_2O,\ \gamma Al_2O_3 - C_2H_6O_2)$ nanofluids in the microchannel at t = 0.5. The heat transfer

coefficient fundamentally evaluates the thermal gradient at the wall and also is a measure of the relative contribution of convection to conductive heat transfer. It is essentially a version of the Nusselt number. The heat transfer rate is strongly dependent on time for both $\left(\gamma Al_2O_3 - H_2O,\ \gamma Al_2O_3 - C_2H_6O_2\right)$ nanofluids. The growth in the magnitude of the heat transfer coefficient for the various values of the Joule heating parameter is presented in **Fig.11.** With increasing Joule heating parameter, the heat transfer coefficient for both $\gamma Al_2O_3 - H_2O, \gamma Al_2O_3 - C_2H_6O_2$ *nanofluids* increases at small axial locations along the microchannel i.e. $x \in [0,\ 0.5]$ whereas at larger axial locations, $x \in [0.5, 1]$, $\boldsymbol{Z}$ decreases. Heat transfer rate is therefore simultaneously sensitive to axial location and time. The deviation of $\boldsymbol{Z}$ for distinct values of nanoparticle volume fraction, χ is presented in **Fig. 12.** The graph shows that elevation in nanoparticle fraction χ stimulates a sizeable enhancement in the absolute value of heat transfer coefficient for both $\gamma Al_2O_3 - H_2O, \gamma Al_2O_3 - C_2H_6O_2$ nanofluids. In **Fig. 13**, it is observed that the heat transfer coefficient exhibits an oscillatory nature, over time for both $\left(\gamma Al_2O_3 - H_2O,\ \gamma Al_2O_3 - C_2H_6O_2\right)$ nanofluids, which is characteristic of peristaltic propulsion regimes. The maximum heat transfer coefficient corresponds to the $\boldsymbol{\gamma Al_2O_3 - water}$ nanofluid and a highly frequently oscillatory behavior is computed for $\gamma Al_2O_3 - ethyleneglycol$nanofluid.

6. CONCLUSIONS

Motivated by new developments in bio-inspired electromagnetic nanofluid microchannel energy applications, a mathematical model has been developed for transient peristaltic electro-osmotic hydromagnetic viscoelastic flow of water based-γAl_2O_3 nanofluids and ethylene glycol-based γAl_2O_3 nanofluids in a microchannel, under the action of mutually orthogonal electrical (axial) and magnetic (transverse) fields. Both magnetohydrodynamic and Joule electrical dissipation effects are included. The robust Jeffreys viscoelastic model is deployed to simulate rheological characteristics and a modified Tiwari-Das nanoscale model used for nanoparticle volume fraction effects. The conservation equations and associated boundary conditions are simplified via lubrication theory and rendered non-dimensionless. Analytic expressions for axial velocity, transverse velocity, stream function, axial pressure gradient and temperature are derived for both

types of nanofluids. MATLAB symbolic software is implemented to evaluate the solutions for physically appropriate data of relevance to bio-inspired electromagnetic rheological nanofluid energy systems. Extensive visualization of the results is presented via graphs. The key finding of the present analysis may be crystallized as follows:

- There is an enhancement in the axial pressure gradient with a reduction in solid fractional volume of nanofluid i.e. nanoparticle percentage doping.
- The axial velocity is suppressed with increasing the strength of the magnetic field and Jeffery rheological parameter whereas it is enhanced with increasing axial electric field and EDL thickness.
- Wall shear stress is strongly dependent on the magnetic field, electric field, Jeffery parameter and the Debye length electro-osmotic parameter.
- Wall heat transfer rates (heat transfer coefficient) for $\gamma Al_2O_3 - ethyleneglycol$ nanofluid are significantly lower than the those computed for $\boldsymbol{\gamma Al_2O_3 - water}$ nanofluid.
- Increasing nanoparticle fraction χ produces a marked enhancement in the absolute value of heat transfer coefficient for both $\gamma Al_2O_3 - H_2O, \gamma Al_2O_3 - C_2H_6O_2$ nanofluids.
- An increase in Helmholtz-Smoluchowski velocity in the negative axial direction physically generates a strong assistive axial electric field which produces enhancement in the wall shear stress magnitudes.
- Wall shear stress increases with greater Grashof number since the axial flow is boosted which manifests in higher shear rates at the microchannel boundaries. In the absence of thermal buoyancy force ($Gr = 0$) i.e. for *forced convection*, shear stress is higher for ($\gamma Al_2O_3 - H_2O$) nanofluid as compared to($\boldsymbol{\gamma Al_2O_3 - C_2H_6O_2}$)nanofluid; however with relatively strong thermal buoyancy present ($Gr > 1$) shear stress for $\left(\gamma Al_2O_3 - C_2H_6O_2\right)$ nanofluid clearly exceeds that for $\left(\gamma Al_2O_3 - H_2O\right)$nanofluid.

- $\boldsymbol{\gamma Al_2O_3 - water}$ nanofluid is more appropriate and efficient for deployment in heat transfer devices and microfluidic systems.

The present study has revealed some interesting features of electromagnetic peristaltic non-Newtonian flows in microchannels for energy systems. However, the two-way, fully coupled interaction of the microchannel walls and the peristaltic propulsion regime have been ignored. Fluid-structure interaction (FSI) may be addressed more comprehensively with commercial

computational fluid dynamics codes such as ANSYS FLUENT [109], COMSOL Multiphysics [110] and ADINA FSI [111]. Efforts in this direction are currently underway.

APPENDIX

The constants as utilized in Eqns. (24)-(33) are as follows.

$$a_1 = \frac{1}{\lambda_1 + 1}\left(306\chi^2 - 0.19\chi + 1\right),\ a_2 = \frac{H^2\left(\lambda_1 + 1\right)}{\left(306\chi^2 - 0.19\chi + 1\right)}\left(\frac{3\chi\left(\sigma - 1\right)}{\sigma - \chi\left(\sigma - 1\right) + 2} + 1\right),$$

$$a_3 = \frac{Gr\left(\lambda_1 + 1\right)}{\left(306\chi^2 - 0.19\chi + 1\right)}\left(\chi\frac{\left(\rho\beta\right)_s}{\left(\rho\beta\right)_{bf}} + 1 - \chi\right),$$

$$a_4 = \frac{U_{HS}\kappa^2\left(\lambda_1 + 1\right)}{\cosh\left(\kappa h\right)\left(306\chi^2 - 0.19\chi + 1\right)},\ a_5 = \frac{\gamma\left(254.3\chi^2 - 3\chi + 1\right)}{\left(28.905\chi^2 + 2.8273\chi + 1\right)}\left(\frac{3\chi\left(\sigma - 1\right)}{\sigma - \chi\left(\sigma - 1\right) + 2} + 1\right),$$

$$a_6 = \frac{\partial p/\partial x}{a_1 a_2^2\cosh\left(a_2 h\right)} - \frac{a_4\cosh\left(\kappa h\right)}{\cosh\left(a_2 h\right)\left(a_2^2 - \kappa^2\right)} + \frac{\mathrm{Pr}_{bf}\, a_3 a_5}{a_2^4\cosh\left(a_2 h\right)} - \frac{a_4 a_7 h}{a_2^2\cosh\left(a_2 h\right)} - \frac{a_8\sinh\left(a_2 h\right)}{\cosh\left(a_2 h\right)} + \frac{\mathrm{Pr}_{bf}\, a_3 a_5 h^2}{2a_2^2\cosh\left(a_2 h\right)},\ a_7 = \frac{2 + \mathrm{Pr}_{bf}\, a_5 h^2}{2h},\ a_8 = -\frac{a_7 a_4}{a_2^3},$$

$$a_9 = \frac{1}{\lambda_1 + 1}\left(123\chi^2 + 7.3\chi + 1\right),\ a_{10} = \frac{H^2\left(\lambda_1 + 1\right)}{\left(123\chi^2 + 7.3\chi + 1\right)}\left(\frac{3\chi\left(\sigma - 1\right)}{\sigma - \chi\left(\sigma - 1\right) + 2} + 1\right),$$

$$a_{11} = \frac{Gr\left(\lambda_1 + 1\right)}{\left(123\chi^2 + 7.3\chi + 1\right)}\left(\chi\frac{\left(\rho\beta\right)_s}{\left(\rho\beta\right)_{bf}} + 1 - \chi\right),$$

$$a_{12} = \frac{\gamma\left(82.1\chi^2 + 3.9\chi + 1\right)}{\left(4.97\chi^2 + 2.72\chi + 1\right)}\left(\frac{3\chi\left(\sigma - 1\right)}{\sigma - \chi\left(\sigma - 1\right) + 2} + 1\right),\ a_{13} = \frac{U_{HS}\kappa^2\left(\lambda_1 + 1\right)}{\cosh\left(\kappa h\right)\left(123\chi^2 + 7.3\chi + 1\right)},$$

$$a_{14}=\frac{\partial p/\partial x}{a_9 a_{10}^2\cosh(a_2 h)}-\frac{a_{13}\cosh(\kappa h)}{\cosh(a_{10}h)\left(a_{10}^2-\kappa^2\right)}+\frac{\mathrm{Pr}_{bf}\,a_{11}a_{12}}{a_{10}^4\cosh(a_2 h)}$$
$$-\frac{a_{13}a_{15}h}{a_{10}^2\cosh(a_{10}h)}-\frac{a_{16}\sinh(a_{10}h)}{\cosh(a_{10}h)}+\frac{\mathrm{Pr}_{bf}\,a_{11}a_{12}h^2}{2a_{10}^2\cosh(a_2 h)},\quad a_{15}=\frac{2+\mathrm{Pr}_{bf}\,a_{12}h^2}{2h},$$

$$a_{16}=-\frac{a_{15}a_{13}}{a_{10}^3}.$$

REFERENCES

[1] E. Serrano *et al*., Nanotechnology for sustainable energy, *Renewable and Sustainable Energy Reviews*, 13, 2373-2384 (2009).

[2] G. Karthik Pandiyan and T. Prabaharan, Implementation of nanotechnology in fuel cells, *Materials Today: Proceedings* (2020). doi.org/10.1016/j.matpr.2020.01.368.

[3] D. Sinton Microfluidics for energy applications, *4th Micro and Nano Flows Conference UCL, London, UK, 7-10 September* (2014).

[4] M.A. Modestino *et al.*, The potential for microfluidics in electrochemical energy systems, *Energy Environ. Sci.*, 9, 3381-3391 (2016).

[5] Ramos, A., *Microfluidic Technologies for Miniaturized Analysis Systems*, Springer, New York, pp. 59–116 (2007).

[6] S.K. Das *et al*, *Nanofluids: Science and Technology*, Wiley, New York (2007).

[7] Xuan, Y. and Li, Q., "Investigation on convective heat transfer and flow features of nanofluids," *ASME J. Heat Transfer*, 125, 151–155 (2003).

[8] M. Kapoor *et al.*, Performance and emission analysis of compression ignition engine with neem methyl ester mixed with cerium oxide (CeO_2) nanoparticles, ASME *J. Energy Resour. Technol*. 142(8): 082308 (2020).

[9] M.A. M. Hassan *et al*., Experimental investigation of the effect of nanofluid on thermal energy storage system using clathrate, ASME *J. Energy Resour. Technol*. 141(4): 042003 (2019).

[10] Q. Zheng *et al.*, Experimental research on titanium dioxide nanofluid in vacuum flash evaporation, *International Journal of Energy Research*, 44 (7) (2020). /doi.org/10.1002/er.5315

[11] D.R. Karana *et al.*, Performance effect on the TEG system for waste heat recovery in automobiles using ZnO and SiO_2 nanofluid coolants, *Heat Transfer—Asian Research*, 48 (1) 216-232 (2019).

[12] H. Reza *et al.*, Energy transfer enhancement inside an annulus using gradient porous ribs and nanofluids, *ASME J. Energy Resour. Technol*. 142(12): 122102 (2020).

[13] H Molavi *et al.,* Applying nanofluid to a rotary disc contactor to investigate breakage phenomenon, *The Canadian Journal of Chemical Engineering,* 90, 672-681 (2012).

[14] Z. Li *et al*., thermo-hydraulic performance of a lubricant containing zinc oxide nanoparticles: a two-phase oil, *ASME J. Energy Resour. Technol*. 142(11): 112107 (2020).

[15] M. Shamshuddin, S.R. Mishra, Ali Kadir and O. Anwar Bég, Unsteady chemo-tribological squeezing flow of magnetized bioconvection lubricants: *numerical study, J. Nanofluids,* 8 (2) 407-419 (2019).

[16] Jayati Tripathi, B. Vasu, Rama S R Gorla, P. V. S. N. Murthy, O. Anwar Bég and P. Saikrishnan, A review on recent advancements in the hemodynamics of nano-drug delivery systems, *Nanoscience and Technology- An International Journal,* 11(1):73–98 (2020).

[17] M. Fatima, A. Sohail, Khush Bakhat Akram, L. Sherin, Saad Ihsan Butt, M. Abid and O. Anwar Bég, Biomechanics of superparamagnetic nanoparticles for laser hyperthermia, *Biomedical Engineering: Applications, Basis and Communications, 32, No. 1 (2020) 2050007 (11 pages) DOI: 10.4015/ S1016237220500076*

[18] B. Vasu, Rama S. R. Gorla, O. Anwar Bég, P. V. S. N. Murthy, V. R. Prasad and A. Kadir, Unsteady flow of a nanofluid over a sphere with non-linear Boussinesq approximation, *AIAA Journal of Thermophysics and Heat Transfer (2018). 13 pages. DOI: 10.2514/1T5516*

[19] M.M. Bhatti, C.M. Khalique, Tasveer Bég, O. Anwar Bég and Ali Kadir, Numerical study of slip and radiative effects on magnetic Fe_3O_4-water-based nanofluid flow from a nonlinear stretching sheet in porous media with Soret and Dufour diffusion, *Modern Physics Letters B 33, 2050026 (24 pages) (2020).*

[20] M.J. Uddin, W.A. Khan, O. Anwar Bég, A.I.M. Ismail, Non-similar solution of g-jitter induced unsteady magnetohydrodynamic radiative slip flow of nanofluid, *Applied Sciences*, 10, 1420, 1-17 (2020).

[21] A. Ahmed *et al*., Use of nanofluids in solar PV/thermal systems, *International Journal of Photoenergy,* Volume 2019, Article ID 8039129, 17 pages (2019).

[22] M. Aneja, Sapna Sharma, S. Kuharat and O. Anwar Bég, Computation of electroconductive gyrotactic bioconvection under nonuniform magnetic field: Simulation of smart bio-nanopolymer coatings for solar energy, *Int. J. Modern Physics B,* 33, 2050028 (22 pages) (2020).

[23] K.S. Reddy *et al.,* Nanofluid and nanocomposite applications in solar energy conversion systems for performance enhancement: a review, *International Journal of Low-Carbon Technologies,* Volume 12, Issue 1, 1-10 (2017).

[24] S. Kuharat, O. Anwar Bég, Ali Kadir and B. Vasu, Computation of metallic nanofluid natural convection in a two-dimensional solar enclosure with radiative heat transfer, aspect ratio and volume fraction effects, *Arabian J. Science and Engineering (2020). (19 pages). doi.org/10.1007/s13369-020-04678-1*

[25] T. Sokhansefat *et al*., Heat transfer enhancement in parabolic trough collector tube using Al_2O_3/synthetic oil nanofluid, *Renew Sustain Energy Rev.* 33, 636-644 (2014).

[26] O. Anwar Bég, S. Kuharat, M. Ferdows, M. Das, A. Kadir, M. Shamshuddin, Magnetic nano-polymer flow with magnetic induction and nanoparticle solid volume fraction effects: *solar magnetic nano-polymer fabrication simulation, Proc. IMechE-Part N: J Nanoengineering, Nanomaterials and Nano-systems (2019).* DOI: 10.1177/ 2397791419838714 (19 pages)

[27] M. Saeedan *et al.,* Numerical thermal analysis of nanofluid flow through the cooling channels of a polymer electrolyte membrane fuel cell filled with metal foam, *International Journal of Energy Research,* 44, 5730-5748 (2020).

[28] M.J. Uddin, W.A. Khan, and O. Anwar Bég, Bioconvection nanofluid slip flow from a wavy surface with applications in nano-biofuel cells *Chin. J. Physics,* 55, 2048-2063 (2017).

[29] Dukhin SS, Deryaguin BV, Electro-kinetic phenomena. In: *Matijevic E (ed) Surface and Colloid Science*. Wiley, New York (1974).
[30] Probstein RF, *Physiochemical Hydrodynamics: An Introduction*. Wiley, New York (1994).

[31] Yang J, Lu FZ, Kostiuk LW, Kwok DY, Electrokinetic microchannel battery by means of electrokinetic and microfluidic phenomena. *J Micromech Microeng* 13(6):963–970 (2003).

[32] Daiguji H, Yang PD, Szeri AJ, Majumdar A., Electrochemomechanical energy conversion in nanofluidic channels. Nano Letters 4(12):2315–2321 (2004).

[33] Jian, Y.J., Liu, Q.S. and Yang, L.G., AC electro-osmotic flow of generalized Maxwell fluids in a rectangular micro-channel," *Journal of Non-Newtonian Fluid Mechanics*, 166, pp. 1304–1314 (2011).

[34] N. Ali, S. Hussain, K. Ullah, O. Anwar Bég, Mathematical modelling of Ellis/Newtonian two-fluid electro-osmotic peristaltic pumping in an axisymmetric tube, *European Physical Journal Plus*, 134, 1-18 (2019).

[35] Richard J Rosa. Magnetohydrodynamic energy conversion, *Hemisphere Pub. Corp, Washington, Engineering Sciences,* Revised edition (1987).

[36] S. Qian and H.H. Bau, Magneto-hydrodynamics based microfluidics, *Mech Res Commun*. 36(1): 10–21 (2009).

[37] Arumugam PU, Fakunle ES, Anderson EC, Evans SR, King KG, Aguilar ZP, Carter CS, Fritsch I. Characterization and pumping–redox magnetohydrodynamics in a microfluidic channel. *Journal of Electrochemical Society*. 153: E185–E194 (2006).

[38] Duwairi, H. and Abdullah, M., Thermal and flow analysis of a magneto-hydrodynamic micropump, *Microsystem technologies*, 13, pp. 33–39 (2007).

[39] Siva Reddy Sheri, O. Anwar Bég, P. Modugula *and* A. Kadir, Computation of transient radiative reactive thermo-solutal magneto-hydrodynamic convection in inclined MHD Hall generator flow with dissipation and cross diffusion, *Computational Thermal Sciences,* 11 (6) 541-563 (2019).

[40] Bau HH, Zhu J, Qian S, Xiang Y. A magneto-hydrodynamic micro fluidic network. Proceedings *ASME International Mechanical Engineering Congress & Exposition; New Orleans, USA.* (2002).

[41] Sara I. Abdelsalam, M. M. Bhatti, A. Zeeshan, A. Riaz and O. Anwar Bég, Metachronal propulsion of magnetized particle-fluid suspension in a ciliated channel with heat and mass transfer, *Physica Scripta,* 94, 115301 (13pp) (2019).

[42] Bao JB, Harrison DJ. Fabrication of microchips for running liquid chromatography by magnetohydrodynamic flow. *The 7th International Conference on Miniaturized Chemical and Biochemical Analysis Systems; October 5-9, 2003; Squaw Valley, California*. pp. 407–410 (2003).

[43] K. Ramesh, D. Tripathi, O. Anwar Bég, Cilia-assisted hydromagnetic pumping of biorheological couple stress fluids, *Propulsion and Power Research*, 8 (3) 221-233 (2019).

[44] M. Shamshuddin, S.R. Mishra, O. Anwar Bég and Ali Kadir, Adomian computation of radiative-convective stretching flow of a magnetic non-Newtonian fluid in a porous medium with homogeneous–heterogeneous reactions, *Int. J Modern Physics B,* 33 (2) (2020). (28 pages).

[45]Zhao, G.P., Jian, Y.J., Chang, L. and Buren, M., Magnetohydrodynamic flow of generalized Maxwell fluids in a rectangular micropump under an AC electric field, *Journal of Magnetism and Magnetic Materials*, 387, 111–117 (2015).

[46] O. Anwar Bég, Tasveer A. Bég, I. Karim, M. S. Khan, M. M. Alam, M Ferdows, M. Shamshuddin, Numerical study of magneto-convective heat and mass transfer from inclined surface with Soret diffusion and heat generation effects: A model for ocean magnetohydrodynamic energy generator fluid dynamics, *Chinese J. Physics,* 60, 167-179 (2019).

[47] Homsy A, Linder V, Lucklum F, de Rooij NF. Magnetohydrodynamic pumping in nuclear magnetic resonance environments. *Sensors and Actuators B.*, 123:636–646 (2007).

[48] G. Nagaraju, J.V. Ramana Murthy, J. Srinivas, O. Anwar Bég and A. Kadir, Second law analysis of flow in a circular pipe with uniform suction and magnetic field effects, *ASME J. Heat Transfer (2018). DOI: 10.1115/1.4041796 (9 pages)*

[49] Z. Asghar, N. Ali, M. Sajid and O. Anwar Bég, Micro-organism swimming propulsion through a shear rate-dependent biorheological fluid in an active channel assisted by a magnetic field, *J. Magnetism and Magnetic Materials (2019).* doi.org/10.1016/j.jmmm.2019.165283 *(13 pages)*

[50] Ibáňez, G. and Cuevas, S., Entropy generation minimization of MHD (magnetohydrodynamic) flow in a microchannel, *Energy*, 35, pp. 4149–4155 (2010).

[51] O. Anwar Bég, A. Zaman, N. Ali, S.A. Gaffar and Eemaan T. A. Bég, Numerical computation of oscillatory two-immiscible magnetohydrodynamic flow in a dual porous media system: FTCS and FEM study, *Heat Transfer Asian Research*, 1-19 (2019). DOI: 10.1002/htj.21429

[52] G. Janardhana Reddy, Bhaskerreddy Kethireddy and O. Anwar Bég, Flow visualization using heat lines for unsteady radiative hydromagnetic micropolar convection from a vertical slender hollow cylinder, *Int. J Mechanical Sciences*, 140, 493-505 (2018).

[53] Jian, Y.J., Si, D.Q., Chang, L. and Liu, Q.S., Transient rotating Electro-magneto-hydrodynamic micropumps between two infinite micro-parallel plates, *Chemical Engineering Science*, 134, pp. 12–22 (2015).

[54] Tso, C.P. and Sundaravadivelu, K., Capillary flow between parallel plates in the presence of electromagnetic field, *Journal of Physics D: Applied Physics*, 34, pp. 3522–3527 (2001).

[55] Si, D.Q. and Jian, Y.J., Electromagnetohydrodynamic (EMHD) micropump of Jeffrey fluids through two parallel microchannels walls with corrugation, *Journal of Physics D: Applied Physics*, 48, 085501 (2015)

[56] Buren, M. and Jian, Y.J., Electromagnetohydrodynamic (EMHD) flow between two transversely wavy micro-parallel plates, *Electrophoresis*, 36, pp. 1539–1548 (2015).

[57] Nguyen, N.T., Micro-magnetofluidics: interactions between magnetism and fluid flow on the microscale, *Microfluid Nanofluid*, 12, pp. 1–16 (2012).

[58] Zhao, G.P., Jian, Y.J. and Li, F.Q., Streaming potential and heat transfer of nanofluids in microchannels in the presence of magnetic field, *Journal of Magnetism and Magnetic Materials*, 407, pp. 75–82 (2016).

[59] Ganguly, S. and Sarkar, S., Thermally developing combined electroosmotic and pressure-driven flow of nanofluid in a microchannel under the effect of magnetic field, *Chemical Engineering Science*, 126, pp. 10–21 (2014).

[60] Sarkar, S. and Ganguly, S., Fully developed thermal transport in combined pressure and electroosmotically driven flow of nanofluid in microchannel under the effect of a magnetic field, *Microfluid Nanofluid*, 18, pp. 623–636 (2015).

[61] G.P. Zhao *et al.,* Electromagnetohydrodynamic flow and heat transfer of nanofluid in a parallel plate microchannel, *J. Mechanics*, 33 (1) 115-124 (2017).

[62] T. Thumma, O. Anwar Bég and A. Kadir, Numerical study of heat source/sink effects on dissipative magnetic nanofluid flow from a non-linear inclined stretching/shrinking sheet, *J. Molecular Liquids*, 232, 159-173 (2017).

[63] J. Mazumdar, *Biofluid Mechanics*, World Scientific, Singapore (1992).

[64] J.C. Burns and T. Parkes, Peristaltic motion, *J. Fluid Mechanics*, 29 (4) 731-743 (1967).

[65] Alim K, Amselem G, Peaudecerf F, Brenner MP, Pringle A Random network peristalsis in *Physarum polycephalum* organizes fluid flows across an individual. *Proc Natl Acad Sci* 110 (33):13306–13311 (2013).

[66] Taber LA, Zhang J, Perucchio R. Computational model for the transition from peristaltic to pulsatile flow in the embryonic heart tube. *ASME J Biomech Eng*. 129(3):441–9 (2007).

[67] Taber LA. Mechanical aspects of cardiac development. *Prog Biophys Mol Biol.* 69(2–3):237–55 (1998).

[68] J. Gjorgjieva *et al.*, Neural circuits for peristaltic wave propagation in crawling *Drosophila* larvae: analysis and modelling, *Front Comput Neurosci*. 7: 24-30 (2014).

[69] Cacciatore T. W., Rozenshteyn R., Kristan W. B., Jr. (2000). Kinematics and modeling of leech crawling: evidence for an oscillatory behaviour produced by propagating waves of excitation. *J. Neurosci*. 20 1643–1655 (2000).

[70] P. Bhovad *et al.*, Peristaltic locomotion without digital controllers: Exploiting multi-stability in origami to coordinate robotic motion, *Extreme Mechanics Letters*, 32, 100552 (2019).

[71] Dodds WJ, Stewart ET, Hodges D, Zboralske FF. Movement of the feline esophagus associated with respiration and peristalsis. An evaluation using tantalum markers. *J Clin Invest.,* 52: 1–13 (1973).

[72] Clouse RE, Staiano A. Topography of the esophageal peristaltic pressure wave. *American J. Physiol Gastrointest Liver Physiol* 261: G677–G684, 1991.

[73] Alla N. Seleznyova and J. Hanan, Mechanistic modelling of coupled phloem/xylem transport for L-systems: combining analytical and computational methods, *Annals of Botany*, 121, 991–1003 (2018).

[74] A. Farina *et al.*, Modeling peristaltic flow in vessels equipped with valves: Implications for vasomotion in bat wing venules, *International Journal of Engineering Science*, 107, 1-12 (2016).

[75] Peristaltic flow of a fluid in a porous channel: A study having relevance to flow of bile within ducts in a pathological state, *International Journal of Engineering Science*, 49, 950-966 (2011).

[76] G. Ravi Kiran, G. Radhakrishnamacharya and O. Anwar Bég, Peristaltic flow and hydrodynamic dispersion of a reactive micropolar fluid: simulation of chemical effects in the digestive process, *J. Mechanics in Medicine and Biology*, 17, 1750013.1-17 (2017).

[77] Yih C. S. and Fung Y.-C. Peristaltic waves in circular cylindrical tubes, ASME *J. Appl. Mech.* 36, 579 – 587 (1969).

[78] Bertuzzi A. and Salinari S., Peristaltic transport of a solid bolus, *J. Biomechanics*, 16 (7) 459 -464 (1983).

[79] Bohme G. B. and Friedrich R., Peristaltic flow of viscoelastic liquids, *J. Fluid Mechanics*, 128, 109-122 (1983).

[80] Takabatake S., Ayukawa K., and Mori A., Peristaltic pumping in circular cylindrical tubes: a numerical study of fluid transport and its efficiency, *J. Fluid Mechanics*, 193, 267 – 283 (1988).

[81] J. Jiménez-Lozano and M. Sen, Streamline topologies of two-dimensional peristaltic flow and their bifurcations, *Chem. Eng. Process.: Process Intensif.*, 49, 704–715 (2010).

[82] T. Ehsan *et al.*, Identification of trapping in a peristaltic flow: A new approach using dynamical system theory, *Physics of Fluids*, 32, 011901 (2020). doi.org/10.1063/1.5128417

[83] M. El Gendy, ANSYS FLUENT CFD simulation of peristaltic micropumps for biomedical engineering, *MSc Dissertation, Aerospace Engineering, September, University of Salford, Manchester, UK* (2016).

[84] J. Prakash, E.P. Siva, D Tripathi, S. Kuharat and O. Anwar Bég, Peristaltic pumping of magnetic nanofluids with thermal radiation and temperature-dependent viscosity effects: *modelling a solar magneto-biomimetic nanopump, Renewable Energy*, 133, 1308-1326 (2019).

[85] V K Narla, Dharmendra Tripathi, O. Anwar Bég and A Kadir, Modelling transient magnetohydrodynamic peristaltic pumping of electroconductive viscoelastic fluids through a deformable curved channel, *Journal of Engineering Mathematics*, 111, 127–143(2018).

[86] V. K. Narla, D. Tripathi and O. Anwar Bég, Electroosmosis-modulated viscoelastic embryo transport in uterine hydrodynamics: mathematical modelling, *ASME J. Biomechanical Engineering* (2018). DOI: 10.1115/1.4041904 (10 pages)

[87] D. Tripathi, S. Bhushan and O. Anwar Bég, Electro-osmotic flow in a microchannel containing a porous medium with complex wavy walls, *J. Porous Media*, 23(5): 477–495 (2020).

[88] D. Tripathi, A. Yadav and O. Anwar Bég, Electro-osmotic flow of couple stress fluids in a micro-channel propagated by peristalsis, *European Physical Journal Plus,* 132: 173-185. (2017).

[89] D. Tripathi, Ashish Sharma and O. Anwar Bég, Electrothermal transport of nanofluids via peristaltic pumping in a finite micro-channel: *effects of Joule heating and Helmholtz-Smoluchowski velocity, Int. J. Heat Mass Transfer,* 111, 138–149 (2017).

[90] Dharmendra Tripathi, Ashish Sharma and O. Anwar Bég, Joule heating and buoyancy effects in electro-osmotic peristaltic transport of nanofluids through a microchannel with complex wave propagation, *Advanced Powder Technology,* 29, 639-653 (2018).

[91] J. Prakash, D. Tripathi, O. Anwar Bég, Comparative study of hybrid nanofluid performance in microchannel slip flow induced by electroosmosis and peristalsis, *Applied Nanoscience (2020).* (14 pages). doi.org/10.1007/s13204-020-01286-1

[92] D. Tripathi, S. Bhushan and O. Anwar Bég, Transverse magnetic field driven modification in unsteady peristaltic transport with electrical double layer effects, *Colloids and Surfaces A: Physicochemical and Engineering Aspects,* 506, 32–39 (2016).

[93] D. Tripathi, R. Jhorar, O. Anwar Bég and A. Kadir, Electro-magneto-hydrodynamic peristaltic pumping of couple stress biofluids through a complex wavy micro-channel, *J. Molecular Liquids,* 236, 358-367 (2017).

[94] J. Prakash, E.P. Siva, D. Tripathi *and* O. Anwar Bég, Thermal slip and radiative heat transfer effects on electro-osmotic magneto-nanoliquid peristaltic propulsion through a microchannel, *Heat Transfer-Asian Research* (2019). 27 pages. DOI: 10.1002/htj.21522

[95] C.V. Pop, S. Fohanno, G. Polidori, C.T. Nguyen, Analysis of laminar-to-turbulent threshold with water γAl_2O_3 and ethylene glycol-γAl_2O_3nanofluids in free convection, in: *Proceedings of the 5th IASME/WSEAS Int. Conference on Heat Transfer, Thermal Engineering and Environment, 188. Athens, Greece, August* 25-27 (2007).

[96] S. Lee, S.U.-S. Choi, S. Li, J.A. Eastman, Measuring thermal conductivity of fluids containing oxide nanoparticles, *ASME J. Heat Transfer* 121, 280–289 (1999).

[97] X. Wang, X. Xu, S.U.-S. Choi, Thermal conductivity of nanoparticles-fluid mixture, AIAA *J. Thermophys. Heat Transfer* 13 (4) 474–480 (1999).

[98] Sidi El Bécaye Maïga *et al*., Heat transfer behaviours of nanofluids in a uniformly heated tube, *Superlattices and Microstructures,* 35, 543-557 (2004).

[99] C. Zhao and C. Yang, Electro-osmotic mobility of non-Newtonian fluids, *Biomicrofluidics,* 5, 014110 (2011).

[100] X. Lu *et al.,* Viscoelastic effects on electrokinetic particle focusing in a constricted microchannel, *Biomicrofluidics*, 9, 014108 (2015).

[101] A. F. Khadrawi *et al*., Basic viscoelastic fluid flow problems using the Jeffreys model, *Chemical Engineering Science*, 60, 7131-7136 (2005).

[102] D. Tripathi and O. Anwar Bég, Mathematical modelling of heat transfer effects on swallowing dynamics of viscoelastic flood bolus through the human oesophagus, *Int. J. Thermal Sciences*, 70, 41-53 (2013).

[103] D. Tripathi, R. Jhorar, O. Anwar Bég, Sachin Shaw, Electroosmosis modulated peristaltic biorheological flow through an asymmetric microchannel: mathematical model, *Meccanica*, 53, 2079–2090 (2018).

[104] Manzoor, K. Maqbool, O. Anwar Bég and S. Shaheen, Adomian decomposition solution for propulsion of dissipative magnetic Jeffrey biofluid in a ciliated channel containing a porous medium with forced convection heat transfer, *Heat Transfer (2018). DOI: 10.1002/htj.21394 (26 pages)*

[105] E. Jiménez *et al*., Start-up electroosmotic flow of Maxwell fluids in a rectangular microchannel with high zeta potentials, *Journal of Non-Newtonian Fluid Mechanics*, 227, 17-29 (2016).

[106] RB. Bird *et al., Dynamics of Polymeric Liquids: Volume I- Fluid Mechanics*, Wiley, USA (1987).

[107] B. Gebhart *et al., Buoyancy-Induced Flows and Transport*, Hemisphere, Washington, USA (1988).

[108] K.C. Cramer and S.I. Pai, *Magnetofluid Dynamics for Engineers and Applied Physicists*, MacGraw-Hill, New York (1973).

[109] B. Vahidi and N. Fatouraee, A biomechanical simulation of ureteral flow during peristalsis using intraluminal morphometric data, *Journal of Theoretical Biology, 298,* 42-50 (2012).

[110] M. Fayaz Ahamed *et al.,* The fluid structure interaction of a peristaltic pump: basics and analysis, *American Journal of Engineering Research*, 5, 12, 155-166 (2020).

[111] J. Degroote, K.J. Bathe and J. Vierendeels, Performance of a new partitioned procedure versus a monolithic procedure in fluid-structure interaction, *Computers and Structures*, 87:793-801 (2009).